

RESEARCH

Open Access



Simplification of KDS 14 Design Method for Slab–Column Connections Subjected to Unbalanced Moment

Ngoc Hieu Dinh¹, Seung-Hee Kim¹ and Kyoung-Kyu Choi^{1*}

Abstract

The current KDS 14 design method yields reasonable accuracy with acceptable safety in assessing the unbalanced moment-carrying capacity of slab–column connections. However, the model requires considerable computational effort owing to the effects of various design parameters, particularly the gravity-load effect. This study proposes a method to simplify the KDS 14 model to evaluate the unbalanced moment-carrying capacity of slab–column connections. In the proposed method, the gravity-load effect is decoupled from equations used for evaluating unbalanced moment-carrying capacity components. Subsequently, the total unbalanced moment-carrying capacity is determined by establishing an interaction between the gravity shear ratio and unbalanced moment components without considering the gravity-load effect. For practical design purposes, final simplified design equations are proposed. The reliability of the simplified method is validated based on a comparison with the current KDS 14 design code using a comprehensive database encompassing interior, exterior, and corner slab–column connections. Furthermore, a parametric study based on the proposed simplified approach, current design codes, combined with finite-element (FE) analysis is performed to elucidate the effects of constituents on the unbalanced moment-carrying capacity of corner slab–column connections. The results show that the proposed simplified model and KDS design method are strongly correlated with the experimental and FE results for a range of design parameters. Meanwhile, the ACI 318 model consistently provides a lower limit for strength prediction, thus yielding overly conservative and safe results compared with the test and FE results in most cases.

Keywords Slab–column connections, Strength model, Eccentric shear, Punching shear strength, Unbalanced moment

1 Introduction

Reinforced concrete flat-plate structures have been adopted increasingly in medium- and high-rise residential building construction owing to their simplicity and efficiency in architectural planning. These structures are characterized by using concrete slabs directly supported

on columns and serve as both the ceiling and floor of a building, thus eliminating the requirements for beams or girders. However, punching shear failure in slab–column connections is a critical issue in the design and performance of flat-plate systems. This type of failure occurs when the applied load exceeds the shear capacity of the slab around the column, thus causing an abrupt brittle failure that can result in significant damage or even structural collapse. Fig. 1 shows an incident of punching shear failure at a slab–column connection, which resulted in a progressive collapse of the entire flat-plate system in the UK in 1997 (Russell, 2015; Wood, 2003). Notably, edge connections are subjected to both gravity

Journal information: ISSN 1976-0485 / eISSN 2234-1315.

*Correspondence:

Kyoung-Kyu Choi
kkchoi@ssu.ac.kr

¹ School of Architecture, Soongsil University, 369 Sangdo-ro, Dongjak-gu, Seoul 153-743, Korea

loads transmitted directly through columns and unbalanced moments originating from various sources such as irregular layouts, differential settlements, and lateral loads. Therefore, additional shear stress is introduced in the connections, thereby significantly increasing the risk of punching shear failure.

The failure mechanism and structural performance of slab–column connections without shear reinforcement subjected to combined gravity loads and unbalanced moments are intricate and depend significantly on factors such as the position of the column in the structural plane (e.g., interior, exterior, and corner connections) (Himawan, 2012; Park et al., 2007), the gravity-load levels (Morrison et al., 1983), and the flexural reinforcement ratio of the slab (Drakatos et al., 2016). The gravity-load level is typically represented by the gravity shear ratio ($V_g/\phi V_n$) between the direct shear force transferred by the critical section around the column and the nominal shear strength of the connections. Extensive experimental and theoretical investigations have been conducted to elucidate the shear behavior of slab–column connections subjected to unbalanced moments. However, the amount of experimental data available for exterior and corner connections is considerably less than that for interior connections. Findings from experiments conducted by Pan and Moehle (1989), Robertson and Johnson (2006), and Tang et al. (2019) showed that an increase in the gravity shear ratio reduced the unbalanced moment-carrying capacity, deformation capacity, and lateral stiffness of interior slab–column connections. However, studies by Stamenkovic and Chapman (1974) and Giduquio et al. (2019) pertaining to corner slab–column connections showed that the unbalanced moment-carrying capacity increased with the gravity shear ratio, as opposed to interior connections. Based on this observation, Moehle

(1988) suggested a bilinear rectangular moment–shear interaction for edge connections. Meanwhile, Robertson and Johnson (2006) and Choi et al. (2007) reported that an increase in the slab flexural reinforcement ratio enhanced the unbalanced moment-carrying capacities and lateral stiffness of slab–column connections but reduce their lateral deformation capacity. Nonetheless, Drakatos et al. (2016) demonstrated that when the gravity shear ratio approached 0.6, the increase in the slab flexural reinforcement ratio minimally affected the unbalanced moment-carrying capacities of slab–column connections experiencing punching shear failure.

In the current design codes, different design approaches are employed to evaluate the unbalanced moment-carrying capacities of slab–column connections in flat-plate systems. The American Code (ACI 318-19, 2019), Chinese Code (GB50010-2019, 2019), and European Code (EC2, 2002) adopted the eccentric shear-stress model, primarily based on test results from interior connections, which were then adjusted for exterior and corner connections. In the design provisions, the eccentric shear stress is assumed to be linearly distributed in the critical section for a simple and practical design. The unbalanced moment-carrying capacity can be indirectly determined from the maximum shear stress in the critical section around the column by assuming a linear moment–shear interaction. Meanwhile, the Korean Standard KDS 14 20 22 (2021) evaluates the unbalanced moment-carrying capacity based on the shear strength model originally developed by Choi et al. (2014). This model determines the unbalanced moment-carrying capacity based on the eccentric shear strength at each face of the critical area around the slab–column connections, i.e., separate from the direct punching shear strength. A summary of design



Fig. 1 Punching shear failure at slab–column connections: Piper’s Row Car Park, Wolverhampton, UK, 1997 (Wood, 2003)

equations based on ACI 318-19 and KDS 14 is provided in Appendix A. Fig. 2 provides a comparison of unbalanced moment-carrying capacity predictions for the existing comprehensive test datasets of slab-column connections (see Tables 1, 2, 3) between ACI 318-19 and KDS 14, where variations in gravity shear ratios ($V_g/\phi V_n$) are considered. In general, KDS 14 demonstrated better and safer predictions than ACI 318-19, irrespective of the gravity shear ratio. Particularly, as shown in Fig. 2b and c, the current design method of ACI 318-19 presents overly conservative predictions

for exterior and corner connections subjected to high levels of the gravity shear ratio ($V_g/\phi V_n > 0.6$).

Despite the advantages of KDS 14 20 22 in comparison to ACI 318-19 for assessing the unbalanced moment-carrying capacities of slab-column connections, the current provision requires considerable computational effort owing to various influencing design parameters. Notably, as listed in Table 5, the calculation procedure is challenging for exterior and corner connections with asymmetrical critical sections, where the existing gravity stress (v_g) transferred by the columns complicates

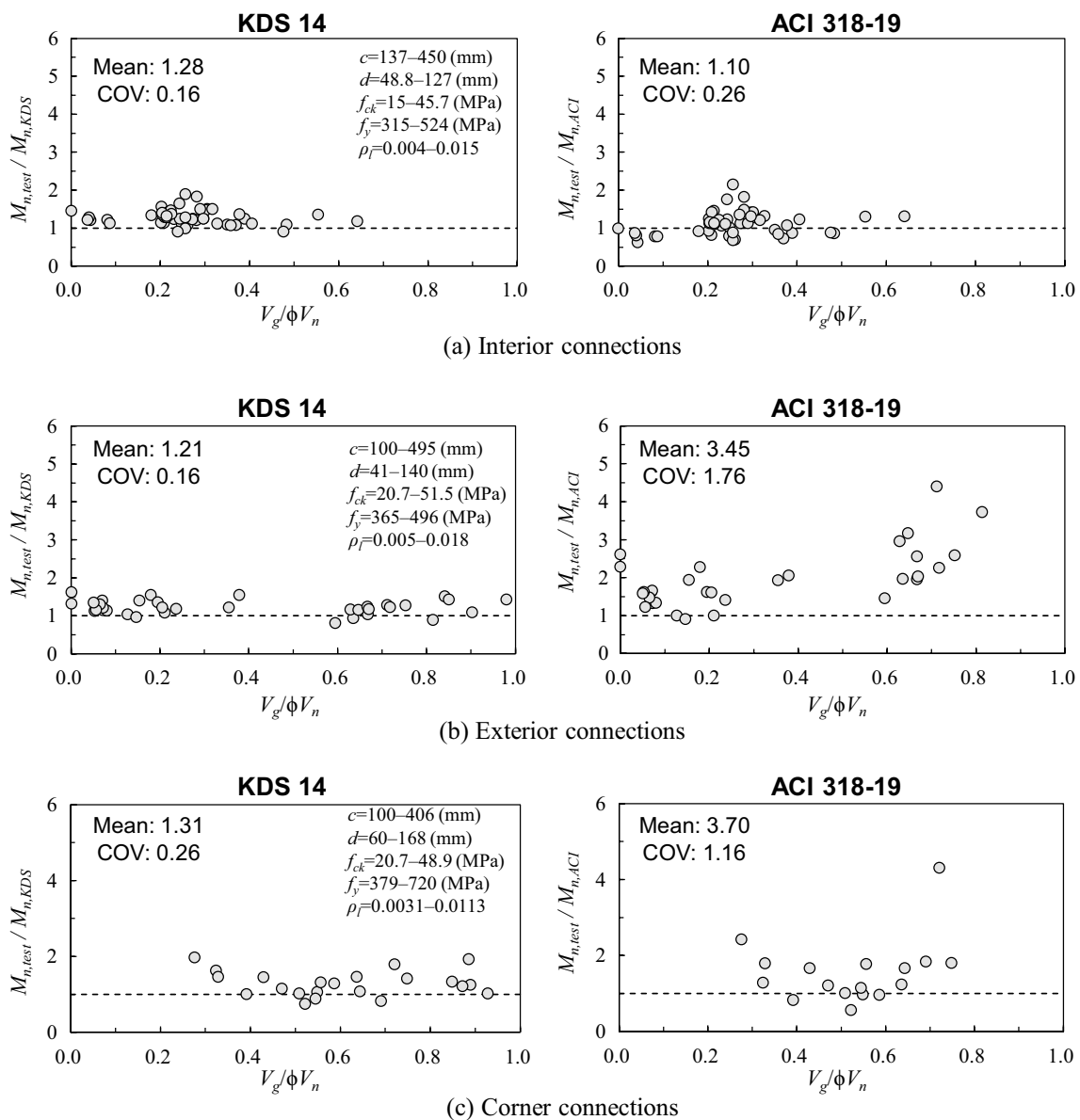


Fig. 2 Unbalanced moment prediction based on KDS 14 and ACI 318-19

Table 1 Properties of interior slab–column connections and predictions of unbalanced moment-carrying capacities

References	Specimens	<i>h</i> (mm)	<i>d</i> (mm)	<i>c</i> ₁ (mm)	<i>c</i> ₂ (mm)	<i>f</i> _{ck} (MPa)	<i>f</i> _y (MPa)	<i>ρ</i> _{lt} (%)	<i>ρ</i> _{lb} (%)	<i>V</i> _g / <i>φV</i> _n	<i>M</i> _{n,test} (kN-m)	<i>M</i> _{n,test} / <i>M</i> _{n,KDS}	<i>M</i> _{n,test} / <i>M</i> _{n,ACI}	<i>M</i> _{n,test} / <i>M</i> _{n,simp}
Pan and Moehle (1992)	Pan1	122	106.3	274	274	33.27	472	0.88	0.35	0.35	61.4	1.09	0.95	1.05
	Pan3	122	106.3	274	274	31.37	472	0.88	0.35	0.20	95.9	1.56	1.25	1.53
Farhey et al. (1993)	Farhey1	80	59.7	300	200	35.10	457.6	0.97	0.55	0.00	36.2	1.45	0.99	1.45
	Farhey3	80	59.7	300	200	15.00	457.6	0.97	0.55	0.27	19.5	1.24	1.13	1.23
	Farhey4	80	59.7	300	120	15.00	457.6	0.94	0.53	0.30	15.5	1.25	1.40	1.24
	S05	120	90	200	400	35.00	458	1.29	0.64	0.28	69.3	1.21	1.82	1.17
Choi et al. (2007)	S1	120	90	300	300	33.50	458	1.01	0.61	0.31	78.5	1.50	1.28	1.46
	S2	120	90	400	200	37.80	458	1.09	0.81	0.30	87.6	1.47	1.42	1.45
	S3	120	90	450	150	33.30	458	0.98	0.66	0.26	106.6	1.89	2.15	1.88
	ND1C	114	100	254	254	29.60	400	0.60	0.10	0.26	39.3	1.08	0.70	1.05
	ND4LL	114	100	254	254	32.30	400	0.60	0.10	0.39	42.3	1.25	0.87	1.21
	ND5XL	114	100	254	254	24.10	400	0.60	0.10	0.48	30.7	1.09	0.86	1.03
	ND6HR	114	100	254	254	26.30	400	1.00	0.30	0.25	54.8	1.22	1.01	1.18
Robertson et al. (2006)	ND7LR	114	100	254	254	18.80	400	0.40	0.10	0.37	27.9	1.08	0.73	1.05
	ND8BU	114	100	254	254	39.20	400	1.00	0.10	0.21	57.0	1.14	0.82	1.11
	L05	152	127	406	406	25.60	469	0.75	0.21	0.25	120.5	1.11	0.79	1.09
	LG05	152	127	406	406	33.20	455	0.75	0.21	0.26	116.1	0.99	0.67	0.97
	LG1	152	127	406	406	27.60	421	1.31	0.21	0.20	156.5	1.14	0.93	1.11
	S1	76.2	60.96	305	305	45.70	322.452	0.65	0.65	0.04	34.2	1.21	0.63	1.21
	S2	76.2	60.96	305	305	35.10	330.031	0.98	0.98	0.04	38.8	1.28	0.81	1.28
	S3	76.2	60.96	305	305	33.90	334.854	1.31	1.31	0.04	41.1	1.21	0.87	1.21
	S4	76.2	60.96	305	305	34.90	319.696	0.98	0.98	0.08	35.5	1.21	0.77	1.21
	S5	76.2	60.96	305	305	35.10	339.677	0.98	0.98	0.18	37.5	1.34	0.91	1.33
Islam and Park	1	88.9	71.12	229	229	27.30	355.524	1.07	1.07	0.23	30.5	1.23	1.06	1.20
	2	88.9	71.12	229	229	31.90	373.438	1.07	1.07	0.22	37.7	1.41	1.20	1.39
	3C	88.9	71.12	229	229	29.70	315.562	1.07	1.07	0.22	35.8	1.47	1.18	1.43
Luo and Durrani	II	114.3	91.44	254	254	20.70	380.328	0.59	0.59	0.09	39.3	1.12	0.78	1.12
	INT1	114.3	91.44	254	254	30.90	417.534	0.55	0.55	0.55	39.2	1.36	1.29	1.31
	INT2	114.3	91.44	254	254	30.70	417.534	0.55	0.55	0.64	31.6	1.18	1.30	1.13
	A12	76.2	60.96	152	152	33.20	372.06	1.50	1.50	0.21	20.4	1.32	1.46	1.28
Hanson and Hanson	A13L	76.2	60.96	152	152	32.80	369.993	1.50	1.50	0.21	19.9	1.29	1.42	1.25
	B16	76.2	60.96	305	152	30.40	340.366	1.50	1.50	0.24	27.3	1.24	1.23	1.22
	C17	76.2	60.96	152	152	36.00	341.055	1.50	1.50	0.24	24.7	1.65	1.76	1.60
	INT	61	48.8	137	137	26.20	434.759	0.65	0.65	0.28	10.3	1.83	1.48	1.79

Table 1 (continued)

References	Specimens	<i>h</i> (mm)	<i>d</i> (mm)	<i>c₁</i> (mm)	<i>c₂</i> (mm)	<i>f_{ck}</i> (MPa)	<i>f_y</i> (MPa)	<i>ρ_{lt}</i> (%)	<i>ρ_{lb}</i> (%)	<i>V_g/φV_n</i>	<i>M_{n,test}</i> (kN-m)	<i>M_{n,test}/M_{n,KDS}</i>	<i>M_{n,test}/M_{n,ACI}</i>	<i>M_{n,test}/M_{n,simp}</i>
Hawkins et al.	S1	152.4	121.9	305	305	34.80	456.807	1.18	1.18	0.27	144.6	1.22	1.35	1.19
	S2	152.4	121.9	305	305	23.40	458.874	0.79	0.79	0.41	87.9	1.12	1.23	1.07
	S3	152.4	121.9	305	305	22.04	461.63	0.51	0.51	0.48	53.7	0.91	0.87	0.88
Durrani and Du	S4	152.4	121.9	305	305	32.30	456.807	1.18	1.18	0.33	125.4	1.12	1.32	1.08
	DNY1	114.3	91.44	254	254	35.30	372.06	0.59	0.59	0.26	47.2	1.28	0.88	1.26
	DNY2	114.3	91.44	254	254	25.70	372.06	0.59	0.59	0.36	33.4	1.07	0.84	1.04
	DNY3	114.3	91.44	254	254	24.60	372.06	0.59	0.59	0.29	48.4	1.50	1.12	1.47
Robertson and Durrani	DNY4	114.3	91.44	254	254	19.10	372.06	0.59	0.59	0.32	44.1	1.50	1.21	1.46
	1	114.3	91.44	254	254	38.00	500.214	0.83	0.83	0.21	64.7	1.28	1.09	1.26
	2C	114.3	91.44	254	254	33.00	500.214	0.83	0.83	0.23	66.2	1.37	1.22	1.35
	3SE	114.3	91.44	254	254	44.00	500.214	0.83	0.83	0.20	72.3	1.36	1.12	1.34
	4S	114.3	91.44	254	254	43.80	500.214	0.83	0.83	0.20	74.0	1.40	1.15	1.38
	5SO	114.3	91.44	254	254	38.00	500.214	0.83	0.83	0.21	66.8	1.32	1.13	1.30
Ghali et al.	SM0.5	152	121.6	305	305	36.80	475.7	0.50	0.50	0.38	100.0	1.36	1.07	1.34
	SM1	152	121.6	305	305	33.40	475.7	1.00	1.00	0.30	132.1	1.24	1.31	1.20
	SM1.5	152	121.6	305	305	40.00	475.7	1.50	1.50	0.24	132.2	0.91	1.11	0.88
										Mean	1.28	1.10	1.25	
										COV	0.16	0.26	0.16	
										<i>P</i> _{0.05}	0.95	0.63	0.92	

h, *d*: thickness and effective depth of slab, respectively; and *c₁*, *c₂*: dimensions of column section; *f_{ck}*: concrete compressive strength; *f_y*: yield strength of reinforcing bars; *ρ_{lt}*, *ρ_{lb}*: top and bottom flexural reinforcement ratio of slab, respectively; *V_g*: direct shear force transmitted to connections; *φV_n*: nominal shear strength determined based on ACI 318-19

Table 2 Properties of exterior slab–column connections and predictions of unbalanced moment-carrying capacities

References	Specimens	h (mm)	d (mm)	c ₁ (mm)	c ₂ (mm)	f _{ck} (MPa)	f _y (MPa)	ρ _{lt} (%)	ρ _{lb} (%)	V _g /φV _n	M _{n, test} (kN-m)	M _{n, test} /M _{n, KDS}	M _{n, test} /M _{n, ACI}	M _{n, test} /M _{n, simp}
Luo and Durant (1995)	IE	115	97	250	250	20.70	380	0.49	0.49	0.13	20.1	1.03	1.00	1.13
	EXT1	115	97	250	250	31.20	418	0.55	0.55	0.15	23.0	0.95	0.91	1.05
	EXT2	115	97	250	250	32.10	418	0.55	0.55	0.21	26.9	1.07	1.00	1.22
Hwang (1990)	b1 (NS)	81	65.2	162.6	162.6	21.80	456	0.64	0.43	0.07	7.6	1.14	1.33	1.21
	b4 (NS)	81	66.8	162.6	162.6	21.80	456	0.62	0.41	0.07	9.6	1.40	1.62	1.49
	c1 (NS)	81	64.8	122	244	21.80	456	0.47	0.47	0.08	6.4	1.13	1.34	1.17
	c4 (NS)	81	66.04	122	244	21.80	456	0.62	0.46	0.07	8.1	1.21	1.66	1.22
	a2 (EW)	81	71.63	162.6	162.6	21.80	444	0.57	0.38	0.07	9.6	1.30	1.48	1.38
Stamenkovic and Chapman (1974)	a3 (EW)	81	72.9	162.6	162.6	21.80	444	0.92	0.37	0.05	10.6	1.12	1.62	1.17
	d2 (EW)	81	70.87	244	122	21.80	444	0.70	0.46	0.06	11.8	1.15	1.23	1.20
	d3 (EW)	81	71.12	244	122	21.80	444	0.92	0.46	0.05	15.2	1.34	1.58	1.38
	C/E/1	76.2	56	127	127	31.50	448	1.09	1.09	1.15	5.6	0.97	— ^a	1.10
	C/E/2	76.2	56	127	127	33.00	496	1.09	1.09	0.84	9.2	1.50	7.44	1.69
Kane (1978)	C/E/3	76.2	56	127	127	34.00	496	1.09	1.09	0.38	10.1	1.54	2.06	1.85
	C/E/4	76.2	56	127	127	27.80	496	1.09	1.09	0.18	8.8	1.54	2.28	1.70
	M/E/2	76.2	56	127	127	26.70	496	1.09	1.09	0.00	8.4	1.61	2.61	1.64
	K-1	50.8	44	100	68	30.20	480	0.99	0.99	0.67	2.4	1.03	2.56	1.13
	K-2	48.01	41	114	75	41.20	480	1.12	1.12	0.64	2.5	0.93	1.97	0.99
Zaghloul (1971)	Z-V(1)	152.4	121	267	267	34.30	474	1.52	1.52	0.63	84.6	1.16	2.96	1.32
	Z-V(2)	152.4	121	267	267	40.50	474	1.72	1.72	0.65	93.6	1.14	3.17	1.30
	Z-V(3)	152.4	121	267	267	38.70	475	1.75	1.75	0.71	103.6	1.28	4.40	1.44
	Z-V(4)	152.4	121	267	267	35.00	437	1.52	1.52	0.00	81.4	1.31	2.29	1.32
	Z-V(6)	152.4	121	267	267	31.30	476	1.52	1.52	0.35	88.1	1.21	1.93	1.41
	Z-V(1)	152.4	121	356	356	26.00	476	1.14	1.14	0.85	106.9	1.42	6.93	1.57
Regan (1981)	SE1	125	98	300	200	35.50	480	1.08	1.08	0.90	39.6	1.09	7.93	1.08
	SE4	125	98	200	300	26.60	480	1.08	1.08	0.81	30.5	0.89	3.73	1.01
	SE7	125	98	200	300	39.80	490	1.08	1.08	0.59	31.8	0.80	1.45	0.94
	SE9	125	98	250	250	41.90	480	0.54	0.54	0.72	35.7	1.22	2.26	1.39
	SE10	125	98	250	250	41.10	480	0.54	0.54	0.67	36.0	1.23	1.95	1.41
Pillai et al. (1982)	SE11	125	98	250	250	51.50	480	0.54	0.54	0.75	39.6	1.27	2.58	1.43
	S1	63.5	50	152	102	38.10	379	0.65	0.65	0.67	4.7	1.17	2.03	1.26
	E1	165.1	130	305	305	22.50	463	0.75	0.75	0.24	67.7	1.17	1.41	1.34
Hawkins et al. (1978)	E2	177.8	140	406	406	29.50	425	1.07	1.07	0.19	150.3	1.35	1.62	1.52
	E3	177.8	140	495	203	22.60	447	1.27	1.27	0.21	126.6	1.22	1.61	1.36
	D15	76.2	57	152	152	31.10	365	1.50	1.50	0.15	10.5	1.39	1.94	1.53

^aNot available

Table 2 (continued)

References	Specimens	h (mm)	d (mm)	c_1 (mm)	c_2 (mm)	f_{ck} (MPa)	f_y (MPa)	ρ_{lt} (%)	ρ_{lb} (%)	$V_g/\phi V_n$	$M_{n, test}$ (kN-m)	$M_{n, test}/M_{n, KDS}$	$M_{n, test}/M_{n, ACI}$	$M_{n, test}/M_{n, simp}$
Sherif (1996)	S1-2	150	114	250	250	29,00	444,3	0,47	0,47	0,98	43,9	1,42	37,05	1,61
								Mean				1,21	3,50	1,33
								COV				0,16	1,72	0,16
								$P_{0,05}$				0,97	-	0,97

h , d : thickness and effective depth of slab, respectively; c_1 , c_2 : dimensions of column section; f_{ck} : concrete compressive strength; f_y : yield strength of reinforcing bars; ρ_{lt} : top and bottom flexural reinforcement ratio of slab, respectively; V_g : direct shear force transmitted to connections; ϕV_n : nominal shear strength determined based on ACI 318-19

^a ACI model cannot predict the unbalanced moment capacity of slab-column connections subjected to high gravity loads

Table 3 Properties of corner slab–column connections and predictions of unbalanced moment-carrying capacities

References	Specimens	<i>h</i> (mm)	<i>d</i> (mm)	<i>c</i> ₁ (mm)	<i>c</i> ₂ (mm)	<i>f</i> _{ck} (MPa)	<i>f</i> _y (MPa)	<i>ρ</i> _{lt} (%)	<i>ρ</i> _{lb} (%)	<i>V</i> _g / <i>φV</i> _n	<i>M</i> _{n, test} (kN-m)	<i>M</i> _{n, test} / <i>M</i> _{n, KDS}	<i>M</i> _{n, test} / <i>M</i> _{n, ACI}	<i>M</i> _{n, test} / <i>M</i> _{n, simp}	
Giduquio et al. (2019)	G1	203	168	406	406	44.90	424.9	0.67	0.33	0.32	110.2	1.62	1.28	1.81	
Cheng and Giduquio (2014)	G3	203	168	406	406	40.30	455.1	0.67	0.33	0.39	70.6	1.01	0.83	1.14	
	R1	203	168	406	406	40.40	478.5	1.00	0.50	0.28	190.5	1.97	2.43	2.07	
	R2	203	168	406	406	39.30	478.5	1.00	0.50	0.43	144.9	1.45	1.67	1.58	
	R3	203	168	406	406	34.10	455.1	1.00	0.50	0.33	134.6	1.47	1.79	1.56	
	S3	140	114	165	165	20.70	379	1.12	1.12	0.93	16.0	1.02	11.36	1.09	
Walker and Regan (1987)	S4	140	114	165	165	35.70	379	1.12	1.12	0.89	22.0	1.25	7.76	1.36	
	SC1	125	100	300	300	43.30	450	0.81	0.81	0.55	25.2	1.07	0.98	1.21	
	SC2	125	100	300	300	47.90	450	0.52	0.52	0.59	24.0	1.29	0.96	1.51	
	SC3	125	100	300	300	37.40	450	1.09	1.09	0.47	31.6	1.15	1.21	1.27	
	SC4	125	100	220	220	40.80	450	0.77	0.77	0.51	16.7	1.02	1.01	1.16	
	SC5	125	100	220	220	46.50	450	1.11	1.11	0.54	18.8	0.89	1.14	0.98	
	SC7	125	100	220	220	43.80	450	1.11	1.11	0.56	27.6	1.32	1.78	1.45	
Desayi and Seshadri (1997)	SC8	80	64	160	160	37.40	595	0.31	0.31	0.75	4.7	1.42	1.80	1.65	
	SC9	80	64	160	160	34.30	595	0.78	0.78	0.64	5.9	1.08	1.67	1.19	
	SC11	80	60	160	160	27.20	595	1.07	1.07	0.69	4.6	0.82	1.84	0.88	
	SC12	80	60	300	300	40.70	595	0.60	0.60	0.64	12.7	1.47	1.24	1.64	
	S101	100	80	100	100	36.00	720	0.57	0.57	0.72	8.8	1.79	4.31	1.96	
	S201	100	80	100	100	36.00	720	0.85	0.85	0.89	12.7	1.93	15.19	2.06	
	S202	100	80	100	100	27.20	720	0.85	0.85	0.85	8.4	1.34	8.67	1.42	
	S302	100	80	100	100	22.40	720	1.13	1.13	0.87	8.8	1.22	11.85	1.28	
												Mean	1.31	3.85	1.44
												COV	0.26	1.16	0.25
												P0.05	0.74	–	0.84

h, *d*: thickness and effective depth of slab, respectively; *c*₁, *c*₂: dimensions of column section; *f*_{ck}: concrete compressive strength; *f*_y: yield strength of reinforcing bars; *ρ*_{lt}, *ρ*_{lb}: top and bottom flexural reinforcement ratio of slab, respectively; *V*_g: direct shear force transmitted to connection; *φV*_n: nominal shear strength determined based on ACI 318-19

the determination of the unbalanced moment-carrying capacity ($M_{T,KDS}$) induced by the eccentric shear stress at the side. This complexity arises from the necessity to establish the neutral-axis locations (c_{N1} and c_{N2}) of the shear-stress distribution based on the force equilibrium while considering the gravity-load effect. Therefore, the current KDS model needs to be simplified further to enhance its applicability in design practices.

In this study, a method is proposed to simplify the KDS 14 design method for evaluating the unbalanced moment-carrying capacities of slab-column connections. In the proposed method, the influence of gravity load is decoupled from equations for evaluating unbalanced moment-carrying capacity components. Subsequently, the total unbalanced moment-carrying capacity is determined by establishing an interaction between the gravity shear ratio and unbalanced moment components without considering the gravity-load effect. Next, simplified design equations are proposed. The reliability of the simplified method is verified by comparing it with the original KDS 14 design code based on a comprehensive database encompassing interior, exterior, and corner slab-column connections. Additionally, a parametric

study combined with finite-element (FE) analysis is performed to elucidate the effects of constituents on the unbalanced moment-carrying capacity of corner slab-column connections.

2 Development of Simplified Method for Slab-Column Connections Subjected to Unbalanced Moment

2.1 Unbalanced Moment-Carrying Capacity Without Considering Gravity-Load Effect

Fig. 3 shows the components of the resisting moment of interior, exterior, and corner slab-column connections based on the KDS 14 design method. The total unbalanced moment-carrying capacity is determined as the summation of three main components: the flexural moment-carrying capacity ($M_{F,KDS}$), the unbalanced moment-carrying capacity due to the eccentric shear at the front/back ($M_{S,KDS}$), and the unbalanced moment-carrying capacity at the sides ($M_{T,KDS}$):

$$M_{n,KDS} = M_{F,KDS} + M_{S,KDS} + M_{T,KDS}. \tag{1}$$

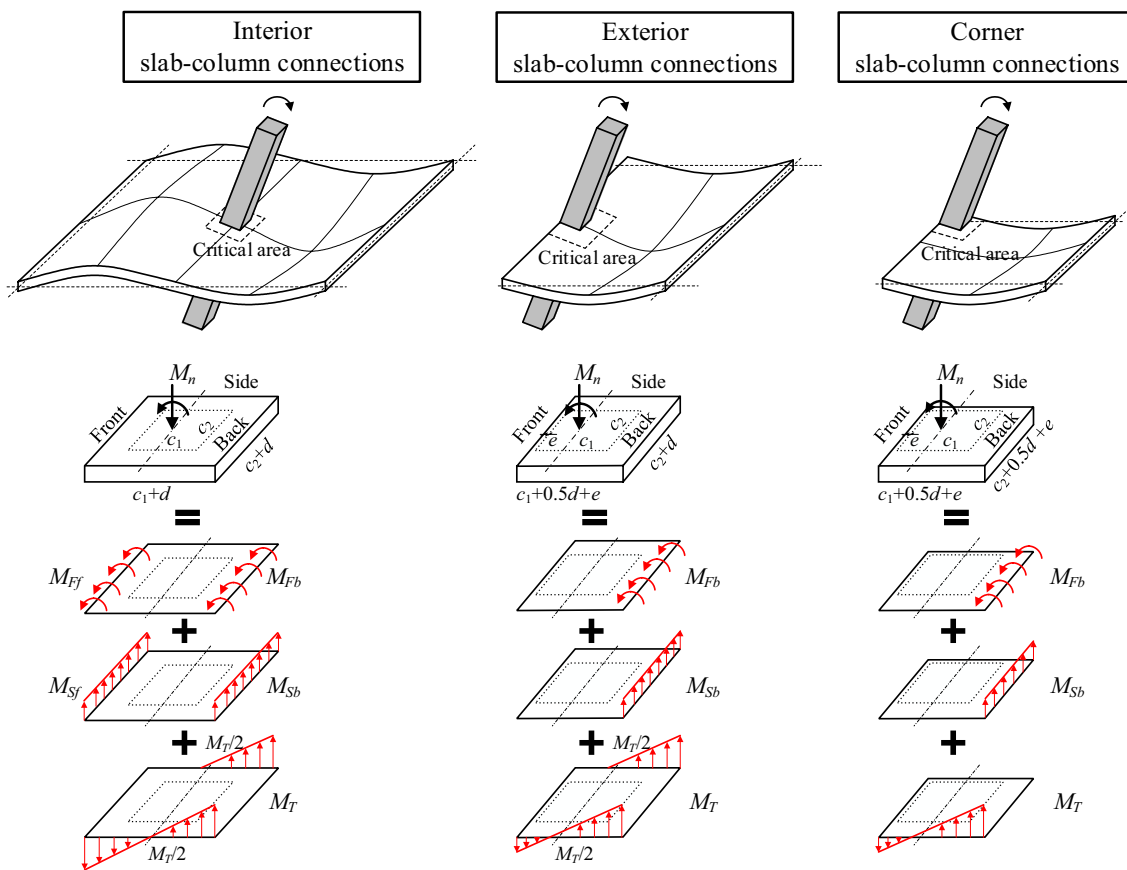


Fig. 3 Components of resisting moments of interior, exterior, and corner slab-column connections

The design equations of KDS 14 20 22 are summarized in detail in Table 5 in the Appendix. In KDS 14 and as shown in Fig. 3, the front and back indicate the faces on which the flexural moment induced by the lateral load is added to or subtracted from the flexural moment induced by the gravity load, respectively, whereas the faces orthogonal to the front and back are defined as the sides. Additionally, owing to the asymmetry of the critical section for exterior and corner slab–column connections, KDS 14 distinguishes the front, back, and side locations based on the load case, as shown in Table 5. Here, E_{1f} and E_{1b} are the load cases in which unbalanced moments whose axes are parallel to the free edge of the slab are added to or subtracted from the unbalanced moment developed by the gravity load, respectively.

As mentioned previously, incorporating gravity stress (v_g) in the design equations requires considerable computational effort. Therefore, in the first phase of the proposed method, the gravity-load effect was decoupled from the components of the unbalanced moment-carrying capacity owing to the eccentric shear at the front/back and sides. Accordingly, the unbalanced moment-carrying capacities at the front/back ($M_{S,o}$) and sides ($M_{T,o}$) without considering v_g are expressed as follows:

- For interior connections:

$$M_{S,o} = [v_n(c_2 + d)](c_1 + d), \tag{2}$$

$$M_{T,o} = \frac{4}{3}v_{n,T} \left(\frac{c_1 + d}{2} \right)^2, \tag{3}$$

where v_n and v_{nT} are the shear stress capacities at the front/back and sides of the connections, respectively (see Table 5 in the Appendix).

- For exterior connections:

Fig. 4 shows the eccentric shear-stress distribution at the sides for the case of exterior connections (load case E_{1f}) based on the KDS 14 model. In the presence of a gravity load (Fig. 4a), the neutral-axis locations (c_{N1} and c_{N2}) of the shear-stress distribution were determined to satisfy the force equilibrium for a specified gravity load (direct shear stress). Therefore, the (c_{N1}/c_{N2}) ratio, based on the analysis of the test database (see Table 2), was strongly correlated with the gravity shear ratio; the higher the gravity shear ratio, the higher was the (c_{N1}/c_{N2}) ratio. Based on KDS 14 (see Eq. (40)), the values of c_{N1} and c_{N2} are to be determined meticulously based on two cases ($c_{N1} \geq c_{N2}$) and ($c_{N1} < c_{N2}$). When the gravity load was not considered (Fig. 4b), owing to the only effect

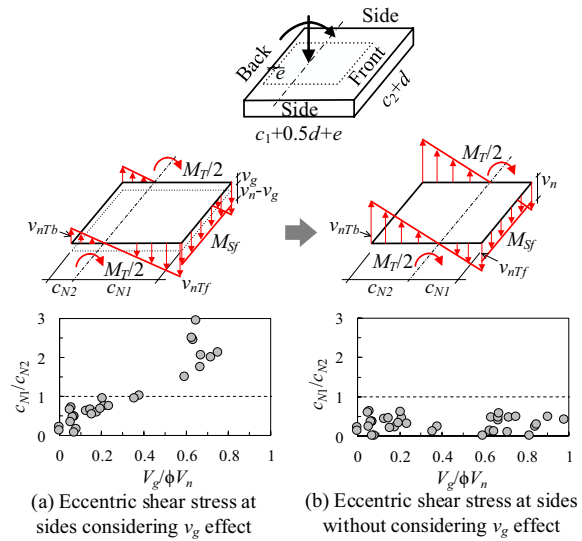


Fig. 4 Eccentric shear stress at sides of exterior slab–column connections with and without considering gravity-load effect

of the shear-stress capacity (v_n) at the front, the neutral axis of the shear-stress distribution consistently deviated toward the front, thus resulting in c_{N1} being less than c_{N2} . Accordingly, $M_{S,o}$ and $M_{T,o}$ can be derived without considering the effect of v_g as follows:

$$M_{S,o} = M_{S,KDS} = 0.5v_n(c_2 + d)d(c_1 + d), \tag{4}$$

$$M_{T,o} = \left[\frac{2}{3}c_{N1} + c_{N2} - \frac{c_1}{2} - e \right] (c_{N1}/c_{N2})v_{nT}dc_{N1} + \left[-\frac{1}{3}c_{N2} + \frac{c_1}{2} + e \right] v_{nT}dc_{N2}, \tag{5}$$

where

$$c_{N1} + c_{N2} = c_1 + 0.5d + e, \tag{6}$$

$$c_{N2} = \frac{v_{nT}(c_1 + 0.5d + e)^2}{v_{nT}(2c_1 + d + e) - v_n(c_2 + d)} \leq c_1 + 0.5d + e. \tag{7}$$

- For corner connections:

Using a similar approach, $M_{S,o}$ and $M_{T,o}$ can be derived for load case E_{1f} without considering the effect of v_g as follows:

$$M_{S,o} = M_{S,KDS} = 0.5v_n(c_2 + 0.5d)d(c_1 + d), \tag{8}$$

$$M_{T,o} = \left[\frac{2}{3}c_{N1} + c_{N2} - \frac{c_1}{2} - e \right] \frac{(c_{N1}/c_{N2})}{2} v_n T d c_{N1} + \left[-\frac{1}{3}c_{N2} + \frac{c_1}{2} + e \right] \frac{v_n T}{2} d c_{N2}, \tag{9}$$

$$c_{N2} = \frac{0.5v_n T (c_1 + 0.5d + e)^2}{v_n T (c_1 + 0.5d + e) - v_n (c_2 + 0.5d)} \leq c_1 + 0.5d + e. \tag{11}$$

where

$$c_{N1} = c_1 + 0.5d + e - c_{N2}, \tag{10}$$

2.2 Interaction Between Gravity Shear Ratio and Unbalanced Moment

In the second phase, considering the effect of gravity load (direct shear stress) on the unbalanced moment-carrying

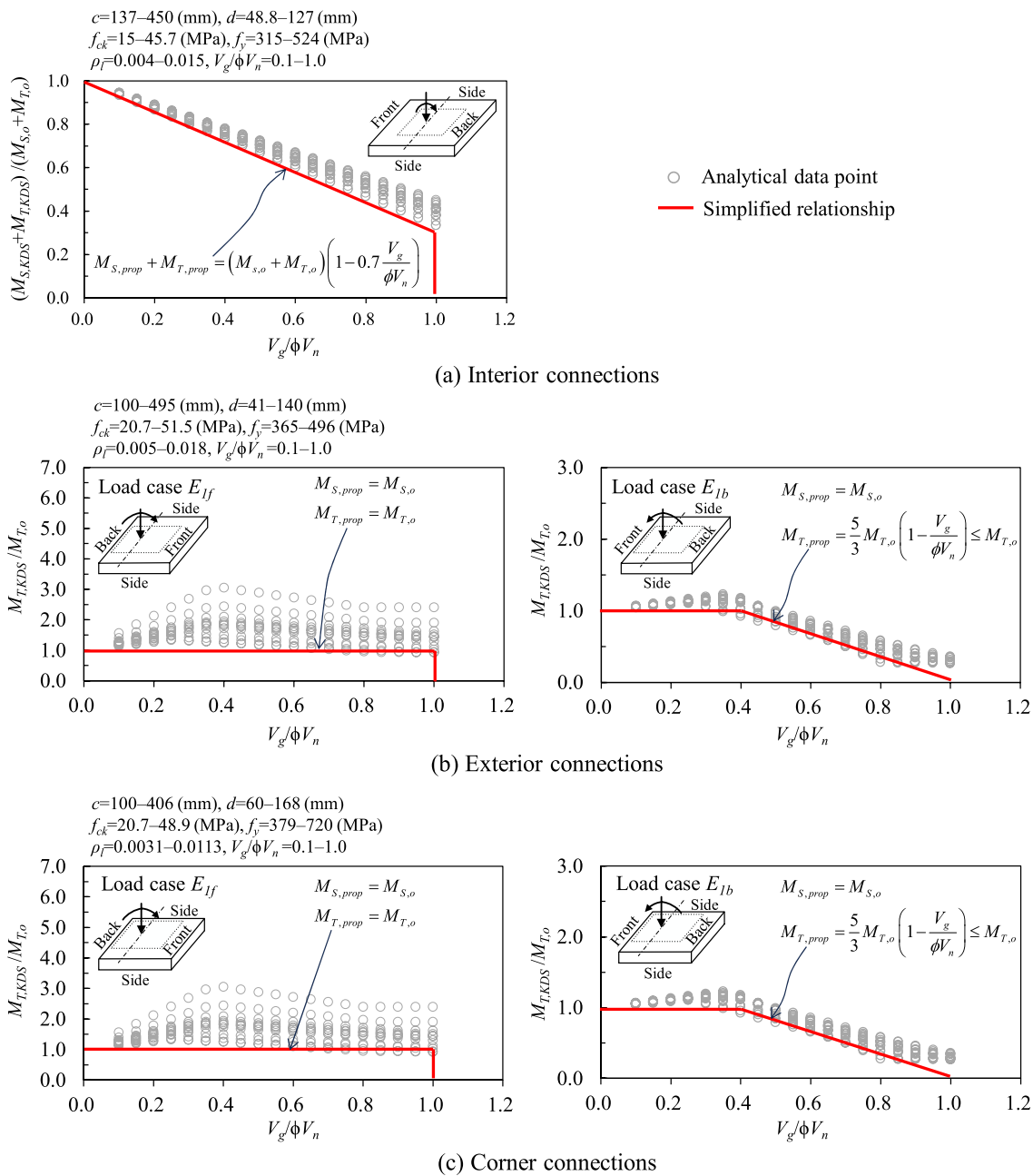


Fig. 5 Gravity shear ratio-normalized unbalanced moment interactions of slab-column connections

capacity of slab–column connections, the relationship between the gravity shear ratio and unbalanced moment without considering the gravity-load effect, as presented in Sect. 2.1, was established. Fig. 5 illustrates the gravity shear ratio-normalized unbalanced moment, which was derived via a parametric study for various types of slab–column connections. The analytical models of the slab–column connections used for the parametric study exhibited identical geometrical and material characteristics with those of the experimental datasets for interior, exterior, and corner connections, as listed in Tables 1, 2, 3. The variable for parametric analysis is the gravity shear ratio ($V_g/\phi V_n$), which ranged from 0.1 to 1.0.

Fig. 5a shows the relationship between $(M_{S,KDS} + M_{T,KDS})$ [see Eqs. (36) and (37)] normalized by $(M_{S,o} + M_{T,o})$ [see Eqs. (2) and (3)] and the gravity shear ratio for the interior connections. For a safe design, the following equation is proposed to determine the total unbalanced moment-carrying capacity of the interior connections, where the gravity-load effect is considered:

$$M_{n,prop} = M_{F,o} + (M_{S,o} + M_{T,o}) \left(1 - 0.7 \frac{V_g}{\phi V_n} \right). \tag{12}$$

Fig. 5b and c shows the relationship between $M_{T,KDS}$ [see Eqs. (40, 43, 46, 49)] normalized by the corresponding $M_{T,o}$ (see Eq. (5)) and the gravity shear ratios for the exterior and corner connections, respectively. For a safe design, the following equation is proposed to determine the unbalanced moment-carrying capacity of the exterior and corner connections while considering the gravity-load effect:

- For load case $E_{I\dot{f}}$

$$M_{n,prop} = M_{F,o} + M_{S,o} + M_{T,o}. \tag{13}$$

- For load case E_{Ib} :

$$M_{n,prop} = M_{F,o} + M_{S,o} + \left(\frac{5}{3} M_{T,o} \left(1 - \frac{V_g}{\phi V_n} \right) \leq M_{T,o} \right). \tag{14}$$

Fig. 6 shows the correlation among the unbalanced moment-carrying capacities of the interior, exterior, and corner connections for various load cases predicted by the KDS 14 design method ($M_{n,KDS}$) and the proposed method ($M_{n,prop}$) using Eqs. (12–14) and the experimental dataset. Furthermore, Fig. 7 shows a comparison of the unbalanced moment-carrying capacity ratios $M_{n,test}/M_{n,prop}$ between the test results and the results predicted based on KDS 14 and the proposed method. In general, the proposed and KDS design methods showed satisfactory agreement.

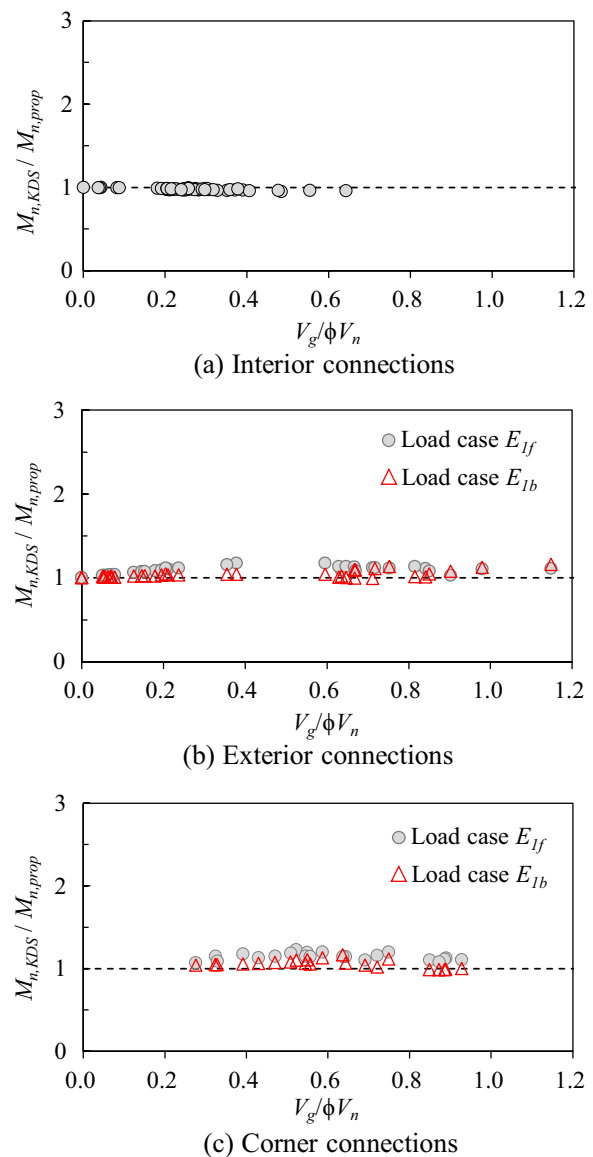


Fig. 6 Comparison between $M_{n,KDS}$ and $M_{n,prop}$

2.3 Simplified Design Equations

In this section, the unbalanced moment-carrying capacities at the sides, without considering the ν_g effect, $M_{T,o}$, are simplified for design purposes. For exterior connections (load case $E_{I\dot{f}}$), Eq. (7) can be reformulated as:

$$\frac{c_{N2}}{c_1 + 0.5d + e} \approx \frac{1}{2 - \frac{\nu_n}{\nu_{n,T}} \left(\frac{c_2 + d}{c_1 + 0.5d} \right)}. \tag{15}$$

Equation (15) suggests that the distance (c_{N2}) from the back to the neutral axis of the shear-stress distribution normalized by the side edge of the critical section ($c_1 + 0.5d + e$) can be presented as a function of the aspect

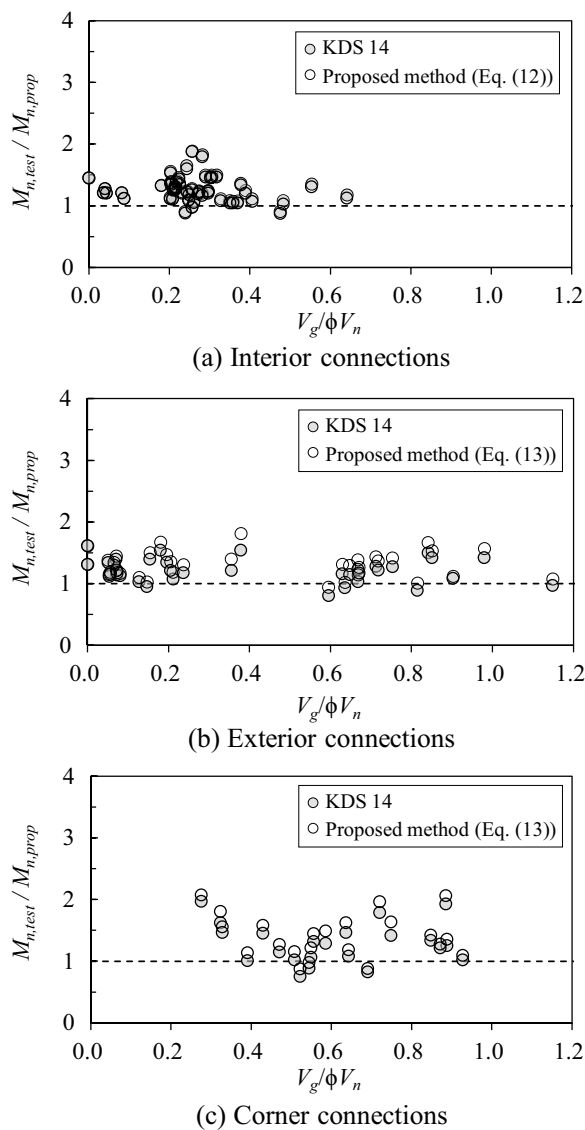


Fig. 7 Unbalanced moment predictions based on KDS 14 and proposed method

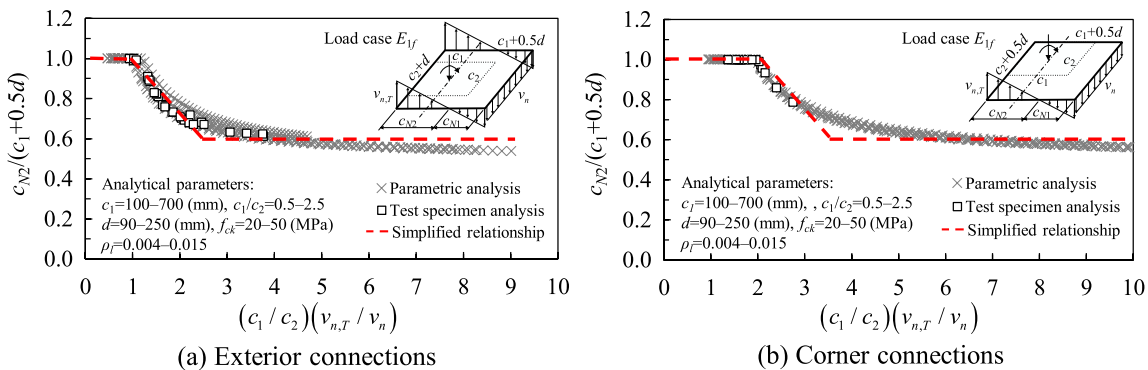


Fig. 8 Relationship between $[c_{N2}/(c_1 + 0.5d)]$ and $[(c_1/c_2)(v_{n,T}/v_n)]$

ratio of the column section (c_1/c_2) and the strength ratio ($v_n/v_{n,T}$) (refer to Table 5). This relationship is depicted in Fig. 8, utilizing a comprehensive parametric study of analytical models of slab–column connections with different design parameters, combined with the analysis results of the test specimens (Tables 2 and 3) for exterior and corner connections. The parametric study incorporated a wide range of design parameters: $c_1=100\text{--}700$ (mm), $c_1/c_2=0.5\text{--}2.5$, $d=90\text{--}250$ (mm), $f_{ck}=20\text{--}50$ (MPa), and $\rho_l=0.004\text{--}0.015$.

Fig. 8 shows that by disregarding the gravity-load effect, as $(c_1/c_2)(v_{n,T}/v_n)$ increased, the normalized distance c_{N2} decreased and converged to approximately 0.6. Based on the relationship $[c_{N1} + c_{N2} = c_1 + 0.5d + e]$, the following simplified equations are derived for exterior connections to determine c_{N1} and c_{N2} for load case E_{1f}

$$c_{N1} = 0.25(c_1 + 0.5d + e) \left[\left(\frac{c_1}{c_2} \right) \left(\frac{v_{n,T}}{v_n} \right) - 1 \right], \tag{16}$$

$$c_{N2} = 0.25(c_1 + 0.5d + e) \left[- \left(\frac{c_1}{c_2} \right) \left(\frac{v_{n,T}}{v_n} \right) + 5 \right], \tag{17}$$

where $1 \leq \left(\frac{c_1}{c_2} \right) \left(\frac{v_{n,T}}{v_n} \right) \leq 2.5$.

The unbalanced moment-carrying capacities at the sides (as expressed in Eq. (9)) can be represented in the following equivalent form:

$$M_{T,o} = \frac{1}{6} \left[v_{nT} + \left(\frac{c_{N1}}{c_{N2}} \right) v_{nT} \right] (c_1 + 0.5d + e) (c_1 - d + 4e)d + 0.5d(d - 2e) \left(\frac{c_{N1}}{c_{N2}} \right) v_{nT} (c_1 + 0.5d + e). \tag{18}$$

By substituting Eqs. (16) and (17) into Eq. (18), the final simplified expression for directly calculating $M_{T,o}$ is as follows:

Table 4 Proposed simplified equations

Interior slab-column connections	Exterior slab-column connections	Corner slab-column connections
<p>For all load directions</p> $M_{n,simp} = M_{F,o} + (M_{S,o} + M_{T,o}) \left(1 - 0.7 \frac{V_o}{\phi V_n}\right)$ $M_{F,o} = \sum A_s f_y j d$ $M_{S,o} = [V_n (C_2 + d)] (c_1 + d) \geq 0$ $V_n = V_c + V_s \leq 0.58 f_{ck} c_u / d$ $M_{T,o} = \frac{4}{3} V_{nT} \left(\frac{c_1 + d}{2}\right)^2 \geq 0$ $V_{nT} = 0.63 \sqrt{f_{ck}} + V_s \leq 0.25 f_{ck}$	<p>Load case E_{1f}</p> $M_{n,simp} = M_{F,o} + M_{S,o} + M_{T,o,simp}$ $M_{F,o} = A_s f_y j d$ $M_{S,o} = 0.5 V_n (C_2 + d) d (c_1 + d) \geq 0$ $V_n = V_c + V_s \leq 0.58 f_{ck} c_u / d$ $M_{T,o,simp} = \frac{1}{6} V_{nT} d (c_1 + 0.5d + e) \left[-3d + 6e + \frac{4(c_1 + 2d - 2e)}{-\left(\frac{c_1}{c_2}\right) \left(\frac{V_{nT}}{V_n}\right) + 5} \right]$ <p>where $1 \leq \left(\frac{c_1}{c_2}\right) \left(\frac{V_{nT}}{V_n}\right) \leq 2.5$</p> <p>Load case E_{1b}</p> $M_{n,simp} = M_{F,o} + M_{S,o} + \left(\frac{5}{3}\right) M_{T,o,simp} \left(1 - \frac{V_o}{\phi V_n}\right) \leq M_{T,o,simp}$ $M_{F,o} = A_s f_y j d$ $M_{S,o} = 0.5 V_n (C_2 + d) d (c_1 + d) \geq 0$ $V_n = V_c + V_s \leq 0.58 f_{ck} c_u / d$ $M_{T,o,simp} = \frac{1}{6} V_{nT} d (c_1 + 0.5d + e) \left[3d - 6e + \frac{4(c_1 - d + 4e)}{-\left(\frac{c_1}{c_2}\right) \left(\frac{V_{nT}}{V_n}\right) + 5} \right]$ <p>where $1 \leq \left(\frac{c_1}{c_2}\right) \left(\frac{V_{nT}}{V_n}\right) \leq 2.5$</p>	<p>Load case E_{1f}</p> $M_{n,simp} = M_{F,o} + M_{S,o} + M_{T,o,simp}$ $M_{F,o} = A_s f_y j d$ $M_{S,o} = 0.5 V_n (C_2 + 0.5d) d (c_1 + d) \geq 0$ $V_n = V_c + V_s \leq 0.58 f_{ck} c_u / d$ $M_{T,o,simp} = \frac{1}{12} V_{nT} d (c_1 + 0.5d + e) \left[-3d + 6e + \frac{4(c_1 + 2d - 2e)}{-\left(\frac{c_1}{c_2}\right) \left(\frac{V_{nT}}{V_n}\right) + 6} \right]$ <p>where $2 \leq \left(\frac{c_1}{c_2}\right) \left(\frac{V_{nT}}{V_n}\right) \leq 3.5$</p> <p>Load case E_{1b}</p> $M_{n,simp} = M_{F,o} + M_{S,o} + \left(\frac{5}{3}\right) M_{T,o,simp} \left(1 - \frac{V_o}{\phi V_n}\right) \leq M_{T,o,simp}$ $M_{F,o} = A_s f_y j d$ $M_{S,o} = 0.5 V_n (C_2 + 0.5d) d (c_1 + d) \geq 0$ $V_n = V_c + V_s \leq 0.58 f_{ck} c_u / d$ $M_{T,o,simp} = \frac{1}{12} V_{nT} d (c_1 + 0.5d + e) \left[3d - 6e + \frac{4(c_1 - d + 4e)}{-\left(\frac{c_1}{c_2}\right) \left(\frac{V_{nT}}{V_n}\right) + 6} \right]$ <p>where $2 \leq \left(\frac{c_1}{c_2}\right) \left(\frac{V_{nT}}{V_n}\right) \leq 3.5$</p>

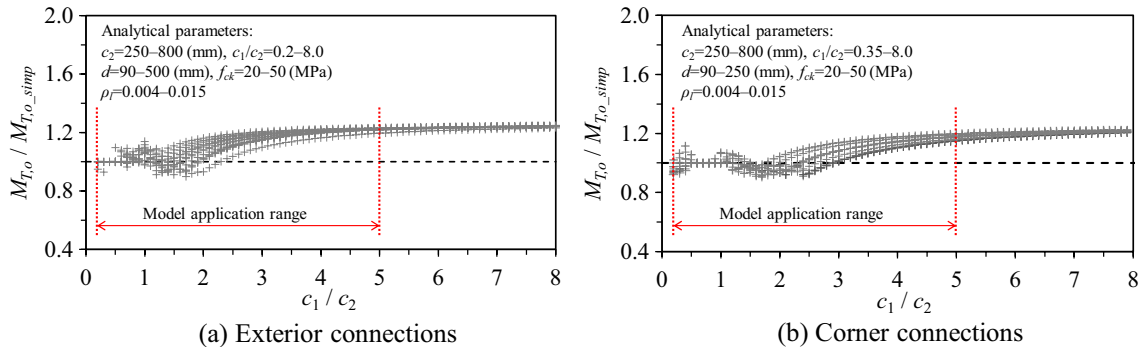


Fig. 9 Relationship between $M_{T,o}/M_{T,o_simp}$ and column aspect ratio

$$M_{T,o_simp} = \frac{1}{6} v_n T d (c_1 + 0.5d + e) \left[-3d + 6e + \frac{4(c_1 + 2d - 2e)}{-\left(\frac{c_1}{c_2}\right)\left(\frac{v_n T}{v_n}\right) + 5} \right] \quad (19)$$

For corner connections, a simplified expression for directly calculating $M_{T,o}$ (load case E_{1p}) can be deduced using a similar approach as follows:

$$M_{T,o_simp} = \frac{1}{12} v_n T d (c_1 + 0.5d + e) \left[-3d + 6e + \frac{4(c_1 + 2d - 2e)}{-\left(\frac{c_1}{c_2}\right)\left(\frac{v_n T}{v_n}\right) + 6} \right], \quad (20)$$

where $2 \leq \left(\frac{c_1}{c_2}\right)\left(\frac{v_n T}{v_n}\right) \leq 3.5$.

The simplified expression for directly calculating the $M_{T,o}$ of the exterior and corner slab–column connections for load case E_{1b} can be determined using a similar methodology. Finally, to present the proposed simplified method, the unbalanced moment-carrying capacity equations are summarized in Table 4 separately for interior, exterior, and corner slab–column connections.

- For interior slab–column connections:

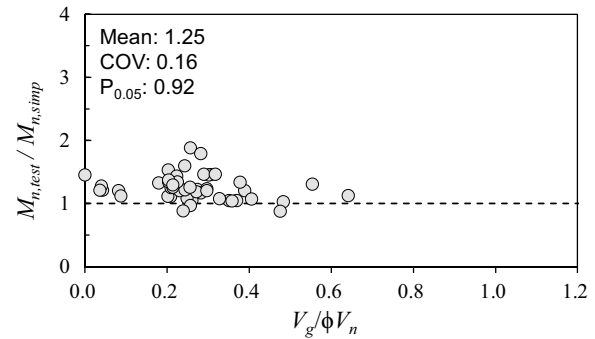
$$M_{n,simp} = M_{F,o} + (M_{S,o} + M_{T,o}) \left(1 - 0.7 \frac{V_g}{\phi V_n} \right). \quad (21)$$

- For exterior and corner slab–column connections:

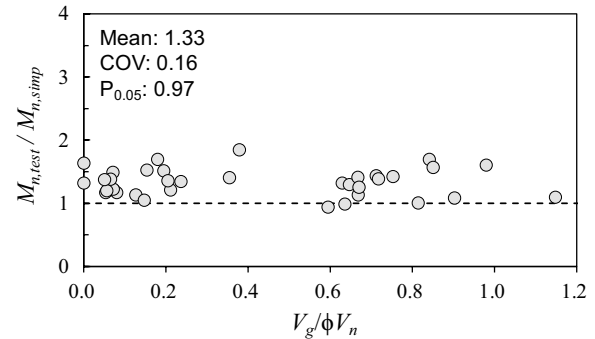
Load case E_{1i} :

$$M_{n,simp} = M_{F,o} + M_{S,o} + M_{T,o_simp}. \quad (22)$$

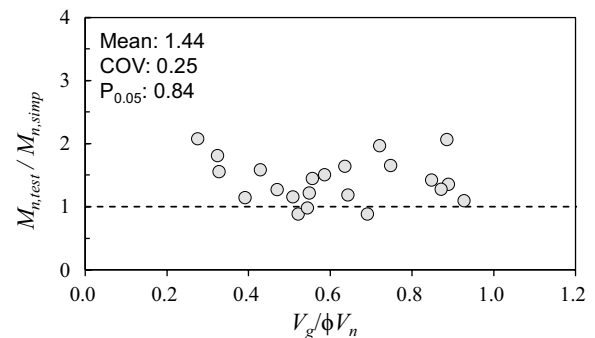
Load case E_{1b} :



(a) Interior connections



(b) Exterior connections



(c) Corner connections

Fig. 10 Unbalanced moment predictions based on simplified method

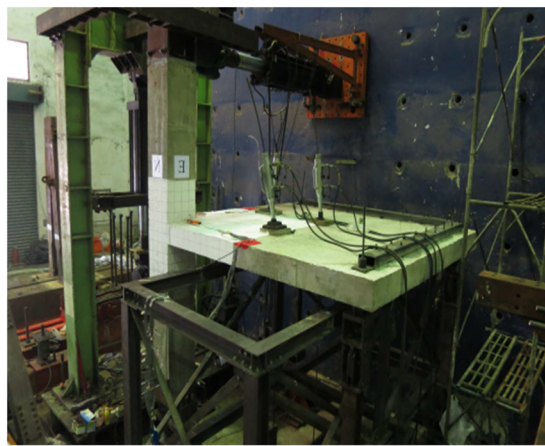
$$M_{n,simp} = M_{F,o} + M_{S,o} + \left(\frac{5}{3} M_{T,o,simp} \left(1 - \frac{V_g}{\phi V_n} \right) \leq M_{T,o,simp} \right). \tag{23}$$

For the application of the proposed simplified model in design practice, Fig. 9 presents the ratio between the unbalanced moment-carrying capacities at the sides ($M_{T,o}$) of the exterior and corner slab-column connections, determined based on the KDS model without considering the gravity load effect and $M_{T,o,simp}$ according to the variation of column aspect ratio (c_1/c_2). As the c_1/c_2 ratio increases, the $M_{T,o}/M_{T,o,simp}$ increases, indicating a pronounced difference between $M_{T,o}$ and $M_{T,o,simp}$. Thus, it is recommended that the applications of the proposed simplified method be limited to the range of column aspect ratio as follows:

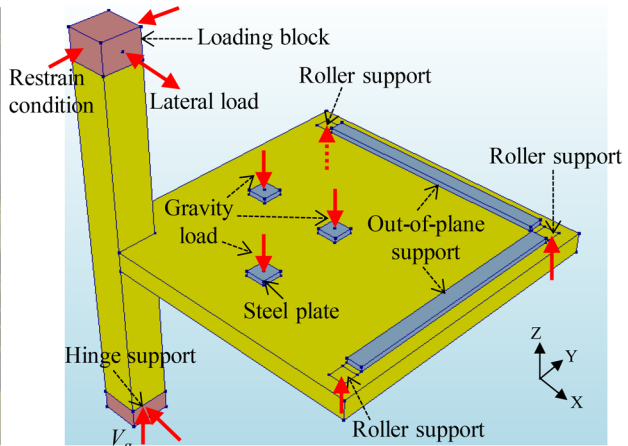
$$\max(c_1/c_2, c_2/c_1) \leq 5. \tag{24}$$

3 Assessment of Simplified Approaches

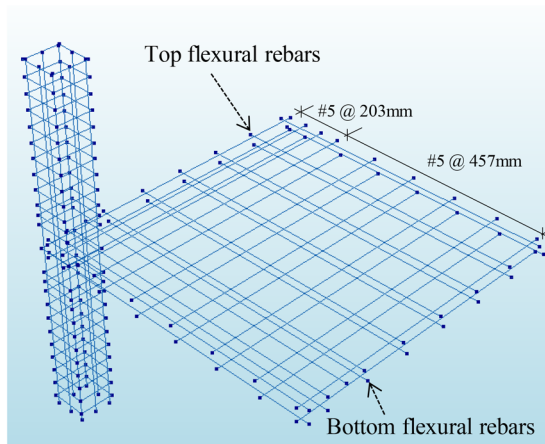
The reliability of the proposed simplified model presented in Table 4 was evaluated by applying to a comprehensive database of slab-column connections collected from previous publication sources (Cheng & Giduquio, 2014; Choi et al., 2007; Giduquio et al., 2019; Luo et al., 1995; Moehle., 1988; Tian et al., 2008). The datasets, which comprised 50 interior connections, 36 exterior connections, and 22 corner connections, are summarized in detail in Tables 1, 2, 3. The data included a wide range of experimental parameters: for interior connections, $137 \text{ mm} \leq c_1 \text{ (or } c_2) \leq 450 \text{ mm}$, $48.8 \text{ mm} \leq d \leq 127 \text{ mm}$, $15 \text{ MPa} \leq f_{ck} \leq 45.7 \text{ MPa}$, $0.004 \leq \rho_l \leq 0.015$, and $315 \text{ MPa} \leq f_y \leq 524 \text{ MPa}$; for exterior connections, $100 \text{ mm} \leq c_1 \text{ (or } c_2) \leq 495 \text{ mm}$, $41 \text{ mm} \leq d \leq 140 \text{ mm}$, $20.7 \text{ MPa} \leq f_{ck} \leq 51.5 \text{ MPa}$, $0.005 \leq \rho_l \leq 0.018$, and $365 \text{ MPa} \leq f_y \leq 496 \text{ MPa}$; and for corner connections, $100 \text{ mm} \leq c_1 \text{ (or } c_2) \leq 406 \text{ mm}$, $60 \text{ mm} \leq d \leq 168 \text{ mm}$,



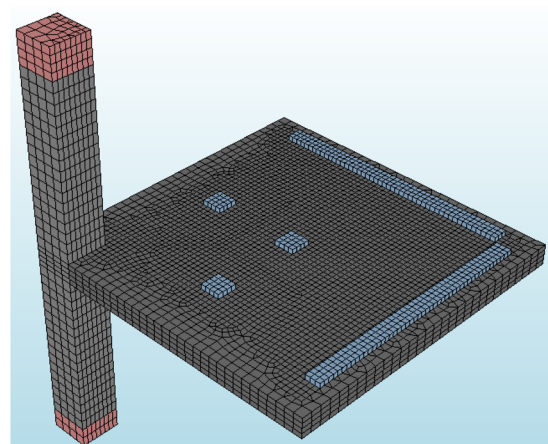
(a) Experimental setup (Giduquio et al., 2019)



(b) Three-dimensional FE model



(c) Reinforcement details



(d) FE mesh

Fig. 11 Three-dimensional FE model of corner slab-column connections

20.7 MPa $\leq f_{ck} \leq 48.9$ MPa, $0.0031 \leq \rho_l \leq 0.0113$, and 379 MPa $\leq f_y \leq 720$ MPa.

The experimental and predicted unbalanced moment-carrying capacities based on the simplified method for different types of slab–column connections are summarized in Tables 1, 2, 3, and a plot of their strength ratios ($M_{n,test}/M_{n,simp}$) against the gravity shear ratio ($V_g/\phi V_n$) is shown in Fig. 10. The 5% fractile ($P_{0.05}$) criterion (CEN, 2002), which is generally accepted as a characteristic value of resistance in limit-state theory (CEN, 2002), was utilized to appraise the safety of the load-bearing units. The closer the 5% fractile value is to unity, the higher is the safety level. It should be noted that for the cases of corner connections, the moment component $M_v = (M_S + M_T)$ caused by eccentric shear is reduced by a factor of 50% to take into account the biaxial effect of applied unbalanced moment, as followed the failure criterion in KDS 14 (refer to Appendix A2).

As shown in Fig. 10, the proposed simplified method can reasonably predict the unbalanced moment-carrying capacity of the slab–column connections listed in Tables 1, 2, 3 with a wide range of gravity shear ratios. Specifically, for interior connections, the obtained mean $M_{n,test}/M_{n,simp}$ ratio was 1.25 and the coefficient of variation was 0.16; correspondingly, for exterior connections, the values were 1.33 and 0.26, respectively, and for corner connections, the values were 1.42 and 0.25, respectively. Compared to the original KDS 14 design method (see Fig. 2), the simplified method maintained a similar accuracy level. Additionally, an acceptable safety level was achieved by adopting the simplified method, as indicated 5% fractile values of 0.92, 0.97, and 0.84 for the interior, exterior, and corner connections, respectively.

4 Parametric Study Using FE Analysis

In this study, a parametric study was performed to analyze the effects of different design parameters on the unbalanced moment capacities of slab–column

connections. Owing to the limited available test data, the case study performed focused on corner connections, which were critically affected by unbalanced moments owing to the geometric asymmetry in both directions. Results from the parametric study using the proposed simplified model were compared with the available limited data as well as with augmented simulation results from FE analysis.

4.1 Finite Element Analysis

4.1.1 Finite Element Model

To investigate the unbalanced moment-carrying capacity of corner slab–column connections, a nonlinear FE model was developed to validate the test program executed by Giduquio et al. (2019). Specimen G1 from this study was chosen for FE analysis due to its exposure to both gravity and lateral cyclic loads, resulting in an unbalanced moment. The loading and boundary conditions of the FE model replicating the experiment are presented in Fig. 11. The FE models were established using the commercial DIANA 10.5 program (Chai & Chai, 2020). The experimental (Giduquio et al., 2019) and simulated test setups are shown in Fig. 10a and b, respectively. The 20-node isoparametric solid brick element (CHX60) available in the DIANA program, which is based on quadratic interpolation and Gaussian integration, was used to simulate the nonlinear behavior of concrete. Meanwhile, a three-dimensional (3D) truss element was employed to model the steel rebar.

As shown in Fig. 11b, the column base was fixed to a steel block mounted on the hinge support, whereas the top of the column was attached to a steel block connected to the deformation support restrained in the X-direction, where lateral loading was generated. Based on the actual test configuration, out-of-plane restraining conditions were imposed at the top of the column to prevent displacement in the transverse direction (Y-direction). For the concrete slab, the three corners were supported

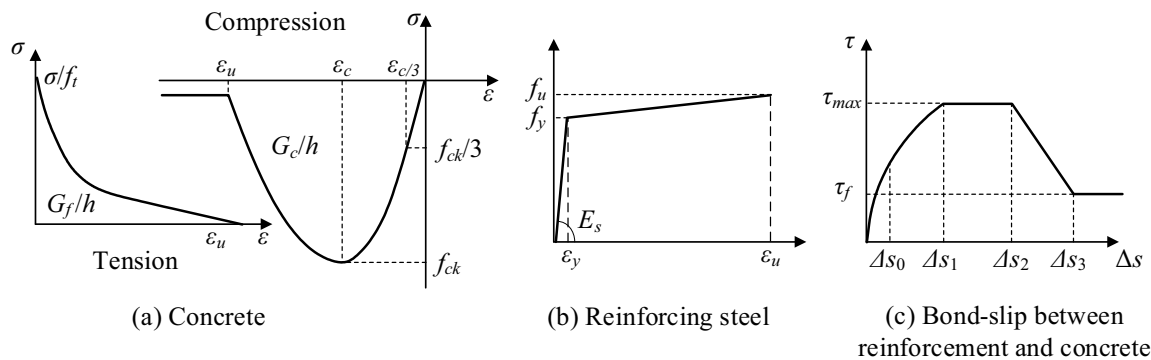


Fig. 12 Material constitutive models used for FE analysis

by roller supports, and the steel plates were sandwiched along the west and east slab edges to prevent out-of-plane deformation. A gravity load was applied to the slab at three loading points affixed to the steel bearing plates. The steel blocks and bearing plates in the FE model were modeled using CHX60 solid elements with the linear elastic behavior of steel.

categories of the total strain crack model, was employed to model the concrete constitutive behavior, based on the assumption that the crack orientation (the principle-strain direction) is fixed during the computational process. To model the concrete behavior in compression, a parabolic curve with the following stress–strain function was adopted in DIANA:

$$\sigma = \begin{cases} -1/3f_{ck}(\varepsilon/\varepsilon_{c/3}) & \text{for } \varepsilon_{c/3} < \varepsilon \leq 0 \\ -1/3f_{ck} \left[1 + 4 \left(\frac{\varepsilon - \varepsilon_{c/3}}{\varepsilon_c - \varepsilon_{c/3}} \right) - 2 \left(\frac{\varepsilon - \varepsilon_{c/3}}{\varepsilon_c - \varepsilon_{c/3}} \right)^2 \right] & \text{for } \varepsilon_c < \varepsilon \leq \varepsilon_{c/3} , \\ -f_{ck} \left[1 - ((\varepsilon - \varepsilon_c)/(\varepsilon_u - \varepsilon_c))^2 \right] & \text{for } \varepsilon_u < \varepsilon \leq \varepsilon_c \end{cases} \quad (25)$$

Fig. 11c shows the reinforcement details of the FE model of specimen G1, which are based on Giduquio et al. (2019). The top and bottom reinforcement ratios were set to 0.67% (rebar #5 @ 203 mm) and 0.33%, respectively, around the slab–column connections within an effective slab width of 711 mm measured from the slab edge. Outside the effective width, the flexural reinforcement spacing was set to 457 mm to satisfy the temperature and shrinkage requirements. Fig. 11d shows the mesh size of the model. In the preliminary analysis, the sensitivity of the mesh size was determined to evaluate the accuracy and efficiency of the FE analysis based on a comparison with the test results. Finally, mesh sizes of 50 mm for the slab and 100 mm for the column were selected to optimize the acceptable accuracy while maintaining the computational timing efficiency.

4.1.2 Material Constitutive Models

The constitutive behavior of concrete is shown in Fig. 12a. The “total strain crack model” available in DIANA was employed to model concrete behavior. This model deals with the average stress–strain approach to obtain the fracture energy within the element, which was established based on the modified compression field theory originally developed by Vecchio and Collins (1986) and further improved by Selby and Vecchio (1995), to extend its applicability to 3D elements. In the study, the “fixed crack model”, which is one of the

where f_{ck} is the concrete compressive strength; and $\varepsilon_{c/3}$, ε_c , and ε_u are strains corresponding to $1/3 f_{ck}$, f_{ck} , and the ultimate stage, respectively. To model the concrete behavior in tension, the Hordijk curve with the following stress–strain function for simulating nonlinear tension softening after cracking was adopted in DIANA:

$$\begin{aligned} \frac{\sigma}{f_t} &= \left[1 + \left(m_1 \frac{\varepsilon}{\varepsilon_u} \right)^3 \right] \cdot \exp \left(-m_2 \frac{\varepsilon}{\varepsilon_u} \right) - (1 + c_1^3) \exp(-m_2) \\ \varepsilon_u &= 5.14 \frac{G_f}{hf_t} \\ G_f &= 0.065 \ln(1 + f_{ck}/10), \end{aligned} \quad (26)$$

where $m_1 = 3.0$ and $m_2 = 6.93$, σ is the normal stress parallel to the crack direction, w_c is the strain when the stress is fully released, G_f is the tensile fracture energy, and f_t is the tensile strength of concrete.

The constitutive behavior of the reinforcement is shown in Fig. 12b. The von Mises yield criterion with isotropic hardening characteristics was used for modeling. The values of yield strength and strain (f_y, ε_y), as well as those of the ultimate strength and strain (f_u, ε_u) were set based on material test results of Giduquio et al. (2019). The bonding behavior between the steel reinforcement and concrete was considered in the modeling based on the bond-slip constitutive model of steel reinforcement, in accordance with the FIB model code 2010 (2010) in DIANA, as depicted in Fig. 12c. The bond-slip equations are as follows:

$$\tau_b = \begin{cases} \tau_{bmax}(\Delta s/\Delta s_1)^\alpha & \text{for } 0 \leq \Delta s \leq \Delta s_1 \\ \tau_{bmax} & \text{for } \Delta s_1 \leq \Delta s \leq \Delta s_2 \\ \tau_{bmax} - (\tau_{bmax} - \tau_{bf})(\Delta s - \Delta s_2)/(\Delta s_3 - \Delta s_2) & \text{for } \Delta s_2 \leq \Delta s \leq \Delta s_3 \\ \tau_{bf} & \text{for } \Delta s_3 < \Delta s \end{cases} \quad (27)$$

where τ_{bmax} is the maximum shear bond stress; τ_b is the local shear bond stress; Δs is the slip displacement (mm); $\Delta s_1 = \Delta s_2 = 0.10$ mm (for hot rolled deformed rebars) is the slip at τ_{bmax} ; and $\Delta s_3 = c_{clear}$, where $c_{clear} [=7$ mm] is the clear distance between ribs. In the FE model, $\tau_{bmax} = 8(f_{ck}/25)^{0.25}$, $\alpha [=0.4]$, and $\tau_{bf} = 0.4\tau_{bmax}$ were adopted based on the FIB model code 2010 (2010) and Tao et al. (2021).

4.2 FE Model Validation

4.2.1 Comparison of Failure Modes and Crack Patterns

Fig. 13 shows a comparison of the crack patterns and failure modes between the FE analysis and experimental results for specimen G1 at a drift ratio of 3%. In general, the FE model reasonably simulated the punching failure from the experiment. At the north and west sides of the specimen (Fig. 13a and b), under the combined gravity load and cyclic lateral load, which caused an unbalanced moment on the connection, severe diagonal cracks with a slope of approximately 30° emerged, as similarly observed in the experimental results. On the top face of the slab (Fig. 13c), critical damage occurred primarily around the column near the top and bottom surfaces, which resulted in the formation of a punching cone. Meanwhile, the bottom face of the slab (Fig. 13d) exhibited numerous fine cracks caused by flexure, accompanied by predominant damage oriented at the critical section around the column.

4.2.2 Comparison of Moment-Carrying Capacities

Fig. 14 shows the FE results of gravity load and unbalanced moment response for specimen G1. The gravity load transferred to the column was determined from the reaction force at the support at the column base in the Z-direction, and the unbalanced moment was calculated as the product of the lateral load at the top of the column and the actual height of the column, based on Giduquio et al. (2019). In the initial phase (Fig. 14a), the gravity load was applied incrementally to the slab until the gravity load ($V_{g,FE}$) transferred to the column reached the specified target $V_{g,test}$ of 109.3 kN, based on the experimental procedure of Giduquio et al. (2019). Subsequently, a horizontal cyclic load was applied, causing unbalanced moments.

Fig. 14b shows the strong correlation between the FE predictions and the test results in terms of the unbalanced moment-drift response, where the difference in

the unbalanced moment capacity between the simulation and test results was 6.3%, at an approximate drift of 1.2%. Additionally, under the damage caused by the increasing unbalanced moment, the connection gradually lost its capacity to transmit the gravity load to the column, which is consistent with the experimental results. Additionally, the prediction results from KDS 14 and the simplified model were presented in this Figure, which exhibited a conservative trend compared to the test results.

4.3 Parametric-Study Results

Fig. 15 presents the parametric-study results obtained using the proposed simplified model to understand the influence of the primary parameters on the unbalanced moment-carrying capacity of corner slab-column connections; the results were compared with the current design codes of KDS 14 and ACI 318-19 and evaluation guidelines ASCE 41-17 (refer to Appendices A1–A3). According to ASCE 41-17 (2017), the unbalanced moment capacities of connections should be calculated as the lesser of the strength determined in accordance with ACI 318 and the flexural strength of the slab section surrounding the column. Parametric analysis was performed for load case E_{1p} whose axes were parallel to the free edge of the slab and added to the unbalanced moment developed by the gravity load.

In Fig. 15a, the influence of the sectional aspect ratio ($c1/c2$) was investigated with variations from 0.45 to 3.0 achieved by adjusting the dimension $c1$ in the loading plane from 182.7 mm to 1218 mm. The other parameters were based on those of G1, which were in fact tested by Giduquio et al. (2019). Overall, both the simplified and KDS 14 models yielded similar conservative results that closely aligned with the experimental and finite element (FE) analysis outcomes. Conversely, the ACI 318-19 model produced unsafe predictions for high aspect ratios, whereas the ASCE 41-17 model demonstrated good agreement with both the test and FE results. For all prediction models, the higher the sectional aspect ratio, the higher the unbalanced capacity of the corner connections. This is because, in both the proposed and KDS 14 models, the unbalanced moment-carrying capacity due to the eccentric shear at the front (M_s) and side (M_T) increased, which was accompanied by an increase in the critical sectional area at the connection (see Eqs. (42) and (43) in the Appendix). In the ACI 318 model [Eq. (33)], the increase in the moment-carrying capacity

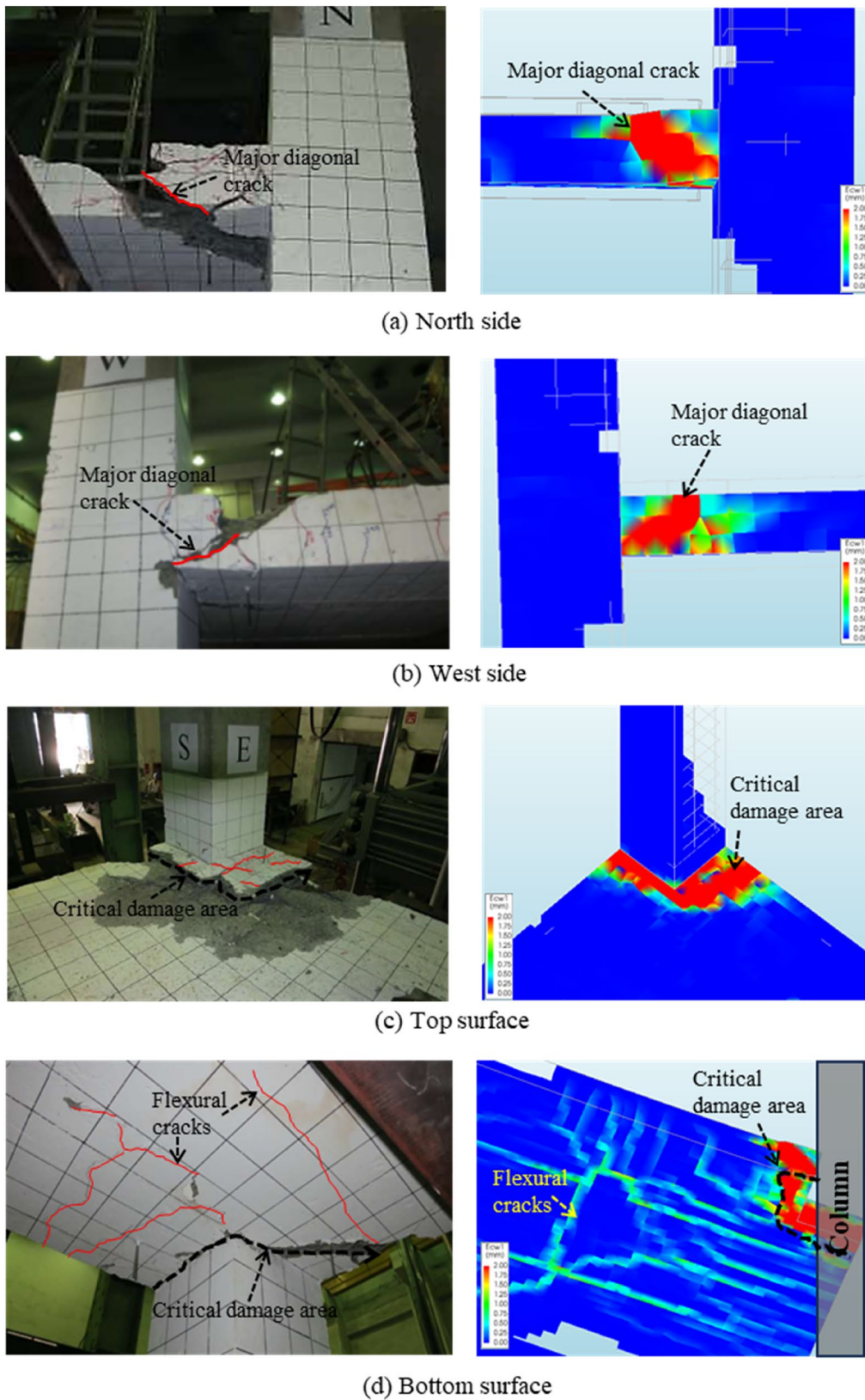


Fig. 13 Comparison between FE analysis and experimental results for failure modes of specimen G1 at 3% drift (Giduquio et al., 2019)

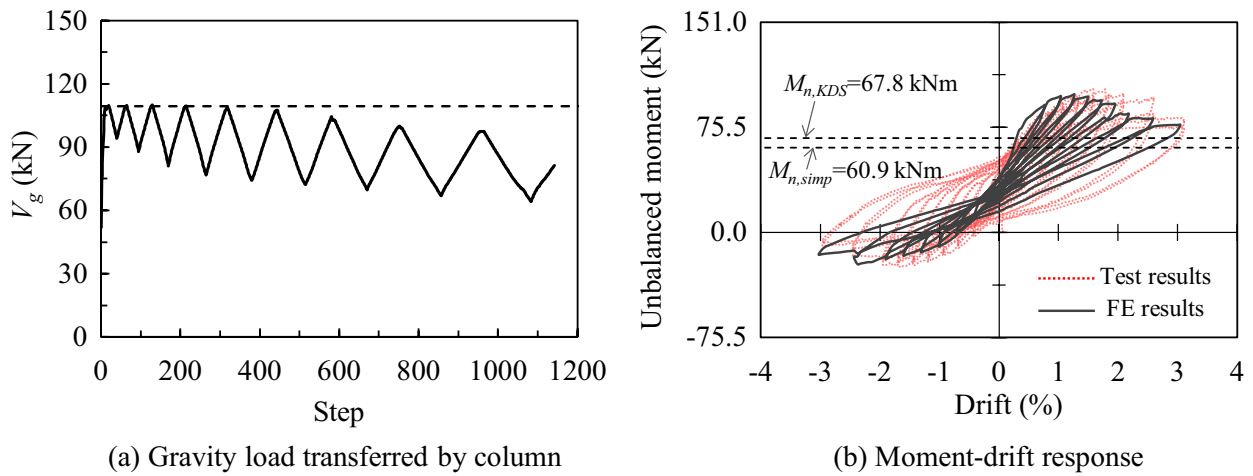


Fig. 14 Comparison between FE analysis and experimental results for shear strengths of specimen G1

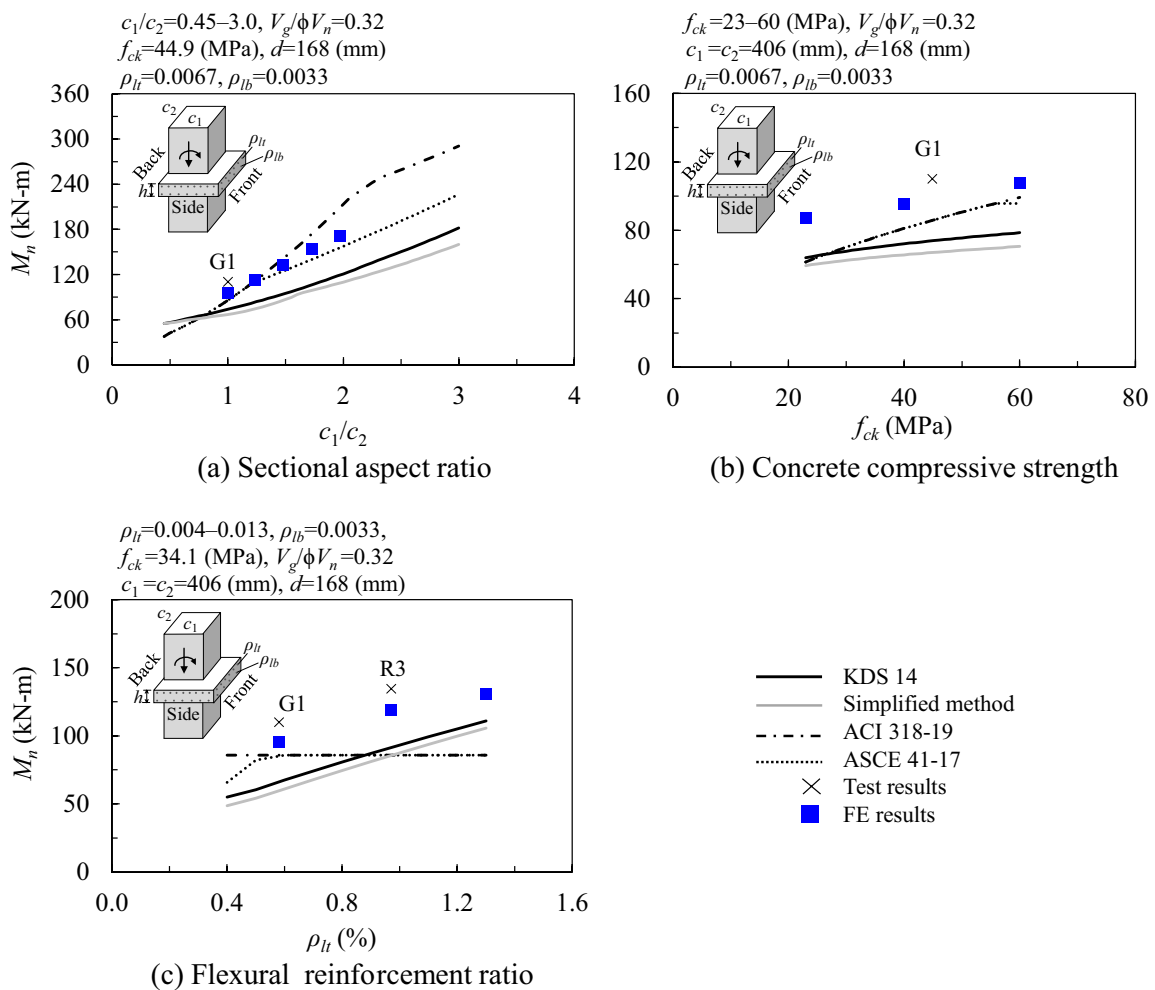


Fig. 15 Parametric-study results

Table 5 Unbalanced moment-carrying capacities based on KDS 14

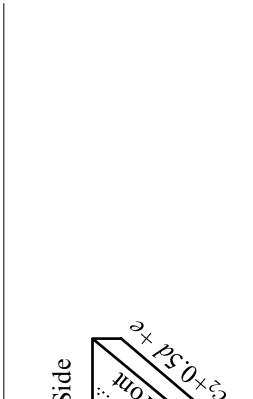
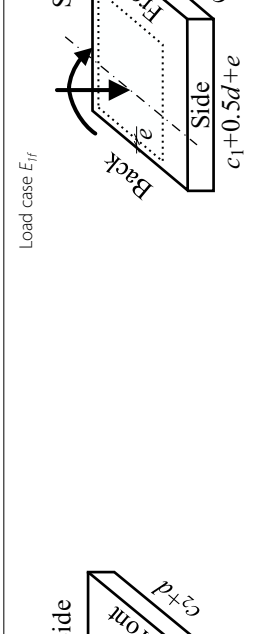
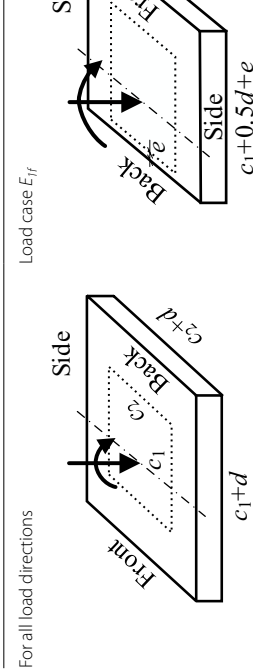
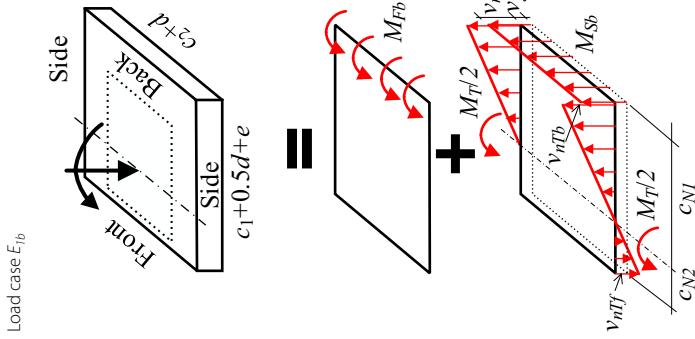
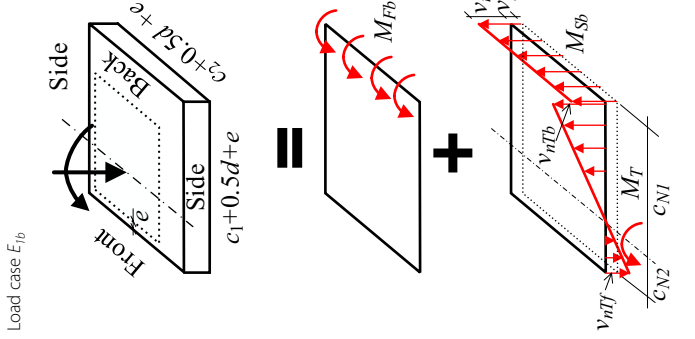
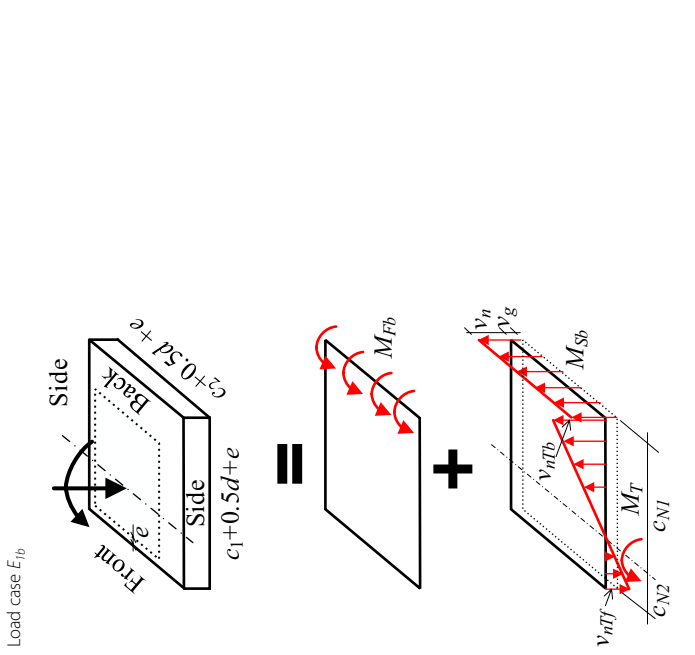
Interior slab-column connections	Exterior slab-column connections	Corner slab-column connections
<p>For all load directions</p> 	<p>Load case E_{1r}</p> 	<p>Load case E_{1r}</p> 
$M_{F,KDS} = M_{Ff} + M_{Pb} = \sum A_s f_y d (35)$ $M_{S,KDS} = [(v_n - v_g)(c_2 + d)d](c_1 + d) \geq 0$ $v_n = v_c + v_s \leq 0.58 f_{ck} c_u / d \quad (36)$ $M_{T,KDS} = \frac{4}{3} (v_{nT} - v_g) \left(\frac{c_1 + d}{2} \right)^2 \geq 0$ $v_{nT} = 0.63 \sqrt{f_{ck}} + v_s \leq 0.25 f_{ck} \quad (37)$	$M_{F,KDS} = M_{Ff} = A_s f_y d (38) \text{ (for exterior connections)}$ $M_{S,KDS} = 0.5 v_n (c_2 + d)d (c_1 + d) \geq 0$ $v_n = v_c + v_s \leq 0.58 f_{ck} c_u / d \quad (39)$ $M_{T,KDS} = [c_{N2} + \frac{2}{3} c_{N1} - \frac{c_1}{2} - e] v_{nT} d c_{N1} + [-\frac{1}{3} c_{N2} + \frac{c_1}{2} + e] v_{nTb} d c_{N2}$ $\text{For } c_{N1} \geq c_{N2}$ $c_{N1} = \frac{v_{nT}(c_1 + 0.5d + e)^2}{v_{nT}(2c_1 + d + e) + v_n(c_2 + d) - v_g b_0} \leq c_1 + 0.5d + e$ $v_{nTf} = v_{nT} \text{ and } v_{nTb} = (c_{N2}/c_{N1})v_{nT}$ $\text{For } c_{N1} < c_{N2}$ $c_{N2} = \frac{v_{nT}(c_1 + 0.5d + e)^2}{v_{nT}(2c_1 + d + e) - v_n(c_2 + d) + v_g b_0} \leq c_1 + 0.5d + e$ $v_{nTf} = (c_{N1}/c_{N2})v_{nT} \text{ and } v_{nTb} = v_{nT}$	$M_{F,KDS} = M_{Ff} = A_s f_y d (41) \text{ (for corner connections)}$ $M_{S,KDS} = 0.5 v_n (c_2 + 0.5d)d (c_1 + d) \geq 0$ $v_n = v_c + v_s \leq 0.58 f_{ck} c_u / d \quad (42)$ $M_{T,KDS} = [c_{N2} + \frac{2}{3} c_{N1} - \frac{c_1}{2} - e] \frac{v_{nT}}{2} d c_{N1} + [-\frac{1}{3} c_{N2} + \frac{c_1}{2} + e] \frac{v_{nTb}}{2} d c_{N2}$ $\text{For } c_{N1} \geq c_{N2}$ $c_{N1} = \frac{0.5 v_{nT}(c_1 + 0.5d + e)^2}{v_{nT}(c_1 + 0.5d + e) + v_n(c_2 + 0.5d) - v_g b_0} \leq c_1 + 0.5d + e$ $v_{nTf} = v_{nT} \text{ and } v_{nTb} = (c_{N2}/c_{N1})v_{nT}$ $\text{For } c_{N1} < c_{N2}$ $c_{N2} = \frac{0.5 v_{nT}(c_1 + 0.5d + e)^2}{v_{nT}(c_1 + 0.5d + e) - v_n(c_2 + 0.5d) + v_g b_0} \leq c_1 + 0.5d + e$ $v_{nTf} = (c_{N1}/c_{N2})v_{nT} \text{ and } v_{nTb} = v_{nT}$

Table 5 (continued)

Interior slab-column connections	Exterior slab-column connections	Corner slab-column connections
<p>Load case E_{fb}</p> 	<p>Load case E_{fb}</p> 	<p>Load case E_{fb}</p> 
<p>$M_{FKDS} = M_{Fb} = A_{sb}f_y/d(44)$ (for exterior connections) $M_{SKDS} = 0.5V_n(c_2 + d)d(c_1 + d) \geq 0$ $V_n = V_c + v_s \leq 0.58f_{ck}c_u/d$ (45)</p>	<p>$M_{FKDS} = M_{Fb} = A_{sb}f_y/d(47)$ (for corner connections) $M_{SKDS} = 0.5V_n(c_2 + 0.5d)d(c_1 + d) \geq 0$ $V_n = V_c + v_s \leq 0.58f_{ck}c_u/d$ (48)</p>	<p>$M_{FKDS} = M_{Fb} = A_{sb}f_y/d(47)$ (for corner connections) $M_{SKDS} = 0.5V_n(c_2 + 0.5d)d(c_1 + d) \geq 0$ $V_n = V_c + v_s \leq 0.58f_{ck}c_u/d$ (48)</p>
<p>$M_{TKDS} = [c_{N2} + \frac{2}{3}c_{N1} - \frac{e}{2}]V_{nTb}dc_{N1} + [-\frac{1}{3}c_{N2} + \frac{e}{2} + e]V_{nT}dc_{N2}$ (49) For $c_{N1} \geq c_{N2}$</p>	<p>$M_{TKDS} = [c_{N2} + \frac{2}{3}c_{N1} - \frac{e}{2} - e] \frac{V_{nTb}}{2} dc_{N1} + [-\frac{1}{3}c_{N2} + \frac{e}{2} + e] \frac{V_{nT}}{2} dc_{N2}$ (49) For $c_{N1} \geq c_{N2}$</p>	<p>$M_{TKDS} = [c_{N2} + \frac{2}{3}c_{N1} - \frac{e}{2} - e] \frac{V_{nTb}}{2} dc_{N1} + [-\frac{1}{3}c_{N2} + \frac{e}{2} + e] \frac{V_{nT}}{2} dc_{N2}$ (49) For $c_{N1} \geq c_{N2}$</p>
<p>$c_{N1} = \frac{V_{nT}(c_1 + 0.5d + e)^2}{V_{nT}(2c_1 + d + e) + V_n(c_2 + d) + v_g b_0} \leq c_1 + 0.5d + e$ $V_{nTf} = (c_{N1}/c_{N2})V_{nT}$ and $V_{nTb} = V_{nT}$ For $c_{N1} < c_{N2}$</p>	<p>$c_{N1} = \frac{V_{nT}(c_1 + 0.5d + e)^2}{V_{nT}(c_1 + 0.5d + e) - V_n(c_2 + 0.5d) + v_g b_0} \leq c_1 + 0.5d + e$ $V_{nTf} = (c_{N1}/c_{N2})V_{nT}$ and $V_{nTb} = V_{nT}$ For $c_{N1} < c_{N2}$</p>	<p>$c_{N1} = \frac{0.5V_{nT}(c_1 + 0.5d + e)^2}{V_{nT}(c_1 + 0.5d + e) - V_n(c_2 + 0.5d) + v_g b_0} \leq c_1 + 0.5d + e$ $V_{nTf} = (c_{N1}/c_{N2})V_{nT}$ and $V_{nTb} = V_{nT}$ For $c_{N1} < c_{N2}$</p>
<p>$c_{N2} = \frac{V_{nT}(c_1 + 0.5d + e)^2}{V_{nT}(2c_1 + 0.5d + e) + V_n(c_2 + d) - v_g b_0} \leq c_1 + 0.5d + e$ $V_{nTf} = V_{nT}$ and $V_{nTb} = (c_{N2}/c_{N1})V_{nT}$</p>	<p>$c_{N2} = \frac{V_{nT}(c_1 + 0.5d + e)^2}{V_{nT}(c_1 + 0.5d + e) + V_n(c_2 + 0.5d) - v_g b_0} \leq c_1 + 0.5d + e$ $V_{nTf} = V_{nT}$ and $V_{nTb} = (c_{N2}/c_{N1})V_{nT}$</p>	<p>$c_{N2} = \frac{0.5V_{nT}(c_1 + 0.5d + e)^2}{V_{nT}(c_1 + 0.5d + e) + V_n(c_2 + 0.5d) - v_g b_0} \leq c_1 + 0.5d + e$ $V_{nTf} = V_{nT}$ and $V_{nTb} = (c_{N2}/c_{N1})V_{nT}$</p>

M_{Fb} : flexural moment capacity at front and back, respectively; A_{sb} : flexural reinforcement area at front and back, respectively; f_y : yield strength of reinforcing bars; V_n : shear stress capacity at front/back and side, respectively; V_{nT} : maximum shear stress at sides intersecting with front and back, respectively; c_{N1} , c_{N2} : distance from neutral axis of shear-stress distribution to outer and inner faces, respectively

was primarily attributed to the increase in the perimeter of the critical section around the column, which consequently increased the polar moment of inertia resisting the eccentric shear stress transferred to the connection caused by the unbalanced moment. Meanwhile, the ASCE 41-17 guidelines [Eqs. (58)] provided more conservative results compared to ACI 318-19 for the case of ($c_1/c_2 > 1$) by selecting the minimum value between strength predicted by the ACI 318 model and the flexural strength of the slab section surrounding the column.

In Fig. 15b, the influence of concrete compressive strength was investigated with variations from 23 to 60 (MPa). The other parameters were based on those of specimen G1, which were in fact tested by Giduquio et al. (2019). The results show that all models considered the effect of concrete compressive strength. As the concrete compressive strength increased, the predicted unbalanced moment-carrying capacity increased as well. Compared with the ACI 318-19 and ASCE 41 model, the proposed and KDS 14 models exhibited a less pronounced effect of increasing compressive strength on the unbalanced moment-carrying capacity, which is consistent with the FE results. This phenomenon was observed because the increase in compressive strength increased the tensile strength of concrete, thus improving the overall shear stress capacity (v_n and v_{nT}) of the critical section but also simultaneously reducing the compression zone depth, as observed when evaluating both the flexural moment resistance at the front [see Eq. (41)] and the two-way nominal shear strength (v_n) [see Eq. (56)].

Fig. 15c shows the effect of the flexural reinforcement ratio on the unbalanced moment-carrying capacity of corner slab-column connections. In both the proposed and KDS 14 models, increasing the top flexural reinforcement ratio from 0.004 to 0.013 correlated with an improvement in the overall unbalanced moment-carrying capacity of the corner connections. This phenomenon arises from the increased flexural moment-carrying capacity at the front (M_F) of the connection with a higher top-reinforcement ratio [see Eq. (41)]. Additionally, the high flexural reinforcement ratio also increased the compression zone when evaluating the maximum capacity of the eccentric shear stress (v_n) at the front, which consequently increased the unbalanced capacity (M_G) owing to the eccentric shear at the front [see Eq. (42)]. The analytical results were consistent with the FE results and the results of specimens G1 and R3 tested by Giduquio et al. (2019), which featured slab-top reinforcement ratios of 0.0058 and 0.0097, respectively. Meanwhile, the ACI 318 model provided a constant strength prediction, indicating insufficient consideration of the effect of flexural reinforcement. In comparison with ACI 318, the ASCE 41 model yielded conservative results for low reinforcement

ratios ($\rho_{lt} < 0.005$), before showing identical results for ($\rho_{lt} \geq 0.005$). This is attributed to the governed strength determined by the eccentricity shear resulting from the combined shear and moment at the connections.

5 Conclusions

An approach for simplifying the KDS 14 design method to assess the unbalanced moment-carrying capacity in slab-column connections was proposed in this study. In the initial step of the proposed method, the gravity-load effect was decoupled from the moment-carrying capacity components due to the eccentric shear at the front/back and sides of the connections, and unbalanced moment-carrying capacity equations were derived. In the subsequent step, considering the gravity-load effect, an interaction was established between the gravity shear ratio and unbalanced moment-carrying capacity components to determine the total unbalanced moment-carrying capacity of different types of slab-column connections.

For design purposes, equations for evaluating the unbalanced moment-carrying capacity at the sides, without considering the gravity-load effect, were simplified for exterior and corner slab-column connections corresponding to different load cases. These equations were derived based on the neutral-axis locations of shear-stress distribution at the sides, which were determined based on the aspect ratio of the column section (c_1/c_2) and the shear strength ratio (v_n/v_{nT}) while disregarding the gravity-load effect.

The reliability of the simplified method was assessed based on large datasets of exterior, interior, and corner slab-column connections with a wide range of design parameters, which were obtained from the literature. The results indicated that the proposed simplified method predicted the unbalanced moment-carrying capacity of slab-column connections with an accuracy level comparable to that of the KDS 14 design method and an acceptable safety level.

A parametric study using the proposed simplified approach and current design codes was conducted to elucidate the effects of selected parameters on the unbalanced moment-carrying capacity of corner slab-column connections. The results from the parametric study were compared with the test results and simulation results yielded by a 3D FE model that was developed and calibrated based on the experimental results. Based on the parametric analysis, both the proposed simplified model and the KDS 14 design method exhibited strong correlations and were conservative with the experimental and FE results for a range of design parameters, including the sectional aspect ratio, concrete compressive strength, and flexural reinforcement ratio of the slab. Meanwhile,

the ACI 318 model consistently provided a lower limit of strength prediction, which yielded overly conservative and safe results compared with the test and FE results in most cases.

Appendix A

Unbalanced Moment-Carrying Capacity Based on Current Design Codes and Guidelines

A1. ACI 318-19

For slab-column connections subjected to combined gravity and unbalanced moments, ACI 318-19 adopts the eccentric shear-stress model to determine the maximum shear stress at a vertex of the control perimeter as follows:

$$v_u = \frac{V_g}{b_o d} \pm \frac{\gamma_v M_u c}{J_c}, \quad (28)$$

where V_g and M_u are the gravity load and unbalanced moment of the connection, respectively; b_o is the perimeter of the critical section located $0.5d$ from each column face; d is the effective depth of the slab; c is the eccentricity of shear stress; J_c is the polar moment of inertia; and γ_v is the fraction of unbalanced moment transferred by the eccentricity of shear, which can be determined as follows:

$$\gamma_v = 1 - \frac{1}{1 + 2/3\sqrt{b_1/b_2}}. \quad (29)$$

The nominal two-way shear stress, v_n , of the slab is determined as follows:

$$v_n = v_c + v_s, \quad (30)$$

$$v_s = \frac{A_v f_{yt}}{b_o s}, \quad (31)$$

where v_c and v_s are the contributions of the concrete and shear reinforcement, respectively; A_v is the shear-reinforcement area on the perimeter peripheral to the column; and f_{yt} and s are the yield strength and spacing of the shear reinforcement, respectively.

$$v_c = \min \left\{ \begin{array}{l} 0.33\lambda_s\lambda\sqrt{f_{ck}} \\ 0.17\left(1 + \frac{2}{\beta}\right)\lambda_s\lambda\sqrt{f_{ck}} \\ 0.083\left(2 + \frac{\alpha_s d}{b_o}\right)\lambda_s\lambda\sqrt{f_{ck}} \end{array} \right\}, \quad (32)$$

where β is the ratio of the long to short sides of the columns; $\alpha_s = 40$ for interior columns, 30 for edge columns, and 20 for corner columns; λ is the modification factor to reflect the reduced mechanical properties of

lightweight concrete relative to normal-weight concrete of the same compressive strength ($\lambda = 1.0$ for normal-weight concrete and $\lambda = 0.75-0.85$ for lightweight concrete); $\lambda_s \left[= \sqrt{2/(1 + 0.004d)} \leq 1, d \text{ is in mm} \right]$ is the size-effect factor; and f_{ck} is the specified compressive strength of concrete.

When punching shear occurs, the maximum shear stress v_u (Eq. (28)) reaches the nominal stress v_n (Eq. (30)). Thus, the unbalanced moment-carrying capacity of the slab-column connection can be derived as follows:

$$M_{n,ACI} = \min \left[(v_n - v_g) \frac{J_c}{c_f \gamma_v}, (v_n + v_g) \frac{J_c}{c_b \gamma_v} \right], \quad (33)$$

where $v_g \left[= V_g/b_o d \right]$ is the gravity shear stress at the critical section.

A2. KDS 14 20 22

See Table 5

In KDS 14 20 22, the punching shear perimeter is defined similarly as in ACI 318-19, with the critical section located $0.5d$ from each column face. The total unbalanced moment-carrying capacity developed at the slab-column connections is determined as the summation of several components at the faces of critical sections, namely, the flexural moment-carrying capacity ($M_{F,KDS}$) at the front/back, the unbalanced moment-carrying capacity ($M_{S,KDS}$) due to the eccentric shear at the front/back, and the unbalanced moment-carrying capacity ($M_{T,KDS}$) at the sides:

$$M_n = M_F + M_S + M_T. \quad (34)$$

In the KDS 14 design method, the moment components are defined differently depending on the connection locations (e.g., interior, exterior, and corner connections) and load cases (e.g., $E_{1\beta}$, E_{1b} , and E_2). The design equations (from 35 to 49) for KDS 14 20 22 are summarized in Table 5.

The nominal two-way shear stress v_n of the slab is determined as follows:

$$v_n = v_c + v_s \leq 0.58f_{ck}c_u/d, \quad (50)$$

$$v_c = k_s k_{b0} \sqrt{f_{te}(f_{te} + 2/3f_{ck})} c_u/d, \quad (51)$$

$$v_s = \frac{A_v f_s}{b_o s}, \quad (52)$$

where v_c and v_s are the contributions of the concrete and shear reinforcement, respectively; f_{te} is the tensile strength of concrete; k_s is the size-effect factor; k_{b0} is the

aspect-ratio factor of the critical section; c_u is the depth of the compression zone; A_v is the shear-reinforcement area on the perimeter peripheral to the column; $f_s [=0.5f_y]$ and s are the tensile stress and spacing of the shear reinforcement, respectively; and f_y is the yield strength of the shear reinforcement.

$$f_{te} = 0.2\sqrt{f_{ck}}, \quad (53)$$

$$k_s = 0.75 \leq \sqrt[4]{300/d} \leq 1.1, \quad (54)$$

$$k_{b0} = \frac{4}{\sqrt{\alpha_s b_o/d}} \leq 1.25, \quad (55)$$

$$c_u = d \left(25\sqrt{\frac{\rho}{f_{ck}}} - 300\frac{\rho}{f_{ck}} \right). \quad (56)$$

At the corner slab-column connections, when the biaxial unbalanced moments are applied, the contribution of the eccentric shear stress to each direction should be decreased because the eccentric shear stress contributes to both unbalanced moments. On the other hand, the contribution of the flexural moments at the connections is independent in each direction. In KDS 14, these aspects are considered for the case of biaxial unbalanced moments by the following failure criteria:

$$\left(\frac{M_{u1} - M_{F1}}{M_{v1}} \right) + \left(\frac{M_{u2} - M_{F2}}{M_{v2}} \right) \leq 1, \quad (57)$$

where M_{u1} and M_{u2} are biaxial unbalanced moments; and $M_{vi} = (M_{Si} + M_{Ti})$.

It should be noted that considering the biaxial unbalanced moment effect, in the strength evaluation of the corner connections in Table 3, the moment component $M_v = (M_S + M_T)$ caused by eccentric shear is reduced by a factor of 50%.

A3. ASCE 41-17

In ASCE 41-17 (2017), it is recommended that the unbalanced moment capacities of connections be calculated as the lesser of the strength considering the eccentricity of shear at the slab-critical section due to the combined shear and moment, in accordance with ACI 318 ($M_{n,ACI}$ in Appendix A1) and the flexural strength of the slab section surrounding the column, as follows:

$$M_{n,ASCE} = \min \left(\sum M_f / \gamma_f, M_{v,ACI} \right), \quad (58)$$

where $\sum M_f$ is the sum of positive and negative flexural strengths of a section of slab within two and one-half slab thicknesses ($2.5h$) from the column edges, and

$\gamma_f [=1/(1+2/3\sqrt{b_1/b_2})]$ is the fraction the moment resisted by flexure, based on ACI 318–19.

Author contributions

N.H.D: conceptualization, methodology, data curation, writing—original draft. S.-H. K: data curation, investigation. K.-K. C: conceptualization, writing—original draft, review and editing, funding acquisition. All authors read and approved the final manuscript

Funding

The authors gratefully acknowledge the financial support provided by the Korean Government through the National Research Foundation of Korea (Grant No. NRF-2022R1A2C2004351), the Brain Pool Program funded by the Ministry of Science and ICT through the National Research Foundation of Korea (Grant No. RS-2023-00218331), and the Earthquake Prevention Safety Human Resource Development Project funded by the Ministry of Public Administration and Security.

Availability of data and materials

The authors declare that the datasets used or analyzed during the current study are available from the corresponding author on reasonable request.

Declarations

Ethics approval and consent to participate

Not applicable.

Consent for publication

Not applicable.

Competing interests

The authors declare no competing interests.

Received: 22 February 2024 Accepted: 13 July 2024

Published online: 18 October 2024

References

- ACI Committee and International Organization for Standardization ACI 318-19. (2019). *Building code requirements for structural concrete and commentary*. American Concrete Institute.
- ASCE 41-17. (2017). *Seismic evaluation and retrofit of existing buildings*. American Society of Civil Engineers.
- CEN. (2002). *EN1990: Eurocode—basis of structural design*. European Commission.
- Chai, S., & Chai, S. (2020). Introduction of DIANA. In S. Chai (Ed.), *Finite element analysis for civil engineering with DIANA software* (pp. 1–67). Berlin: Springer. <https://doi.org/10.1007/978-981-15-2945-0>
- Cheng, M. Y., & Giduquio, M. B. (2014). Experimental study of corner slab-column connection. *ACI Structural Journal*, 111(5), 1123. <https://doi.org/10.14359/51686817>
- Choi, K.-K., Shin, D. W., & Park, H. G. (2014). Shear-strength model for slab-column connections subjected to unbalanced moment. *ACI Structural Journal*. <https://doi.org/10.14359/51686533>
- Choi, M. S., Cho, I. J., Han, B. S., Ahn, J. M., & Shin, S. W. (2007). Experimental study of interior slab-column connections subjected to vertical shear and cyclic moment transfer. *Key Engineering Materials*, 348, 641–644. <https://doi.org/10.4028/www.scientific.net/KEM.348-349.641>
- Desayi, P., & Seshadri, H. K. (1997). Punching shear strength of flat slab corner column connections. Part 1. Reinforced concrete connections. *Proceedings of the Institution of Civil Engineers-Structures and Buildings*, 122(1), 10–20. <https://doi.org/10.1680/istbu.1997.29163>
- Drakatos, I. S., Muttoni, A., & Beyer, K. (2016). Internal slab-column connections under monotonic and cyclic imposed rotations. *Engineering Structures*, 123, 501–516. <https://doi.org/10.1016/j.engstruct.2016.05.038>

- Eurocode 2 (EC 2). (2002). *Design of concrete structures—Part I: General rules and rules for buildings*. European Committee for Standardization.
- Farhey, D. N., Adin, M. A., & Yankelovsky, D. Z. (1993). RC flat slab-column subassemblages under lateral loading. *Journal of Structural Engineering*, 119(6), 1903–1916. [https://doi.org/10.1061/\(ASCE\)0733-9445\(1993\)119:6\(1903\)](https://doi.org/10.1061/(ASCE)0733-9445(1993)119:6(1903))
- Fédération Internationale du Béton (FIB). 2010. Model code for concrete structures.
- GB50010-2019. (2019) Code for design of concrete structures. Ministry of Housing and Urban-Rural Development of the PRC and General Administration of Quality Supervision Inspection and Quarantine.
- Giduquio, M. B., Cheng, M. Y., & Dlamini, L. S. (2019). Reexamination of strength and deformation of corner slab-column connection with varied slab reinforcement ratio. *ACI Structural Journal*, 116(2), 53–63. <https://doi.org/10.14359/51712276>
- Hanson, N. W., & Hanson, J. M. (1968). *Shear and moment transfer between concrete slabs and columns* (p. 16). Portland Cement Association, Research and Development Laboratories.
- Hawkins, N. M., Wong, C. F., & Yang, C. H. (1978). *Slab edge column connections transferring high intensity reversing moments normal to the edge of the slab*. Department of Civil Engineering, University of Washington.
- Himawan, S. A. S. (2012). *Shear strength of slab-column connections under gravity and cyclic lateral loading* (Doctoral dissertation). <https://doi.org/10.32657/10356/50515>
- Hwang, S. J. (1990). *An experimental study of flat-plate structures under vertical and lateral loads*. Report No. UCB/SEM-90/11, University of California, Berkeley
- Kane, K. A. (1978). Some model tests on the punching action of reinforced concrete slabs at edge columns. *Honours project, The Queen's University of Belfast*.
- Korea Concrete Institute (KCI). (2021). Design code for shear and torsion of concrete structures (KDS 14 20 22), Korea Design Standard (KDS), Ministry of Land, Infrastructure, and Transport of Korea, Seoul, Republic of Korea (in Korean).
- Luo, Y. H., & Durrani, A. J. (1995). Equivalent beam model for flat-slab buildings—part II: exterior connections. *Structural Journal*, 92(2), 250–257. <https://doi.org/10.14359/1154>
- Moehle, J. P. (1988). Strength of slab-column edge connections. *Structural Journal*, 85(1), 89–98. <https://doi.org/10.14359/2995>
- Morrison, D. G., Hirasawa, I., & Sozen, M. A. (1983). Lateral-load tests of R/C slab-column connections. *Journal of Structural Engineering*, 109(11), 2698–2714. [https://doi.org/10.1061/\(ASCE\)0733-9445\(1983\)109:11\(2698\)](https://doi.org/10.1061/(ASCE)0733-9445(1983)109:11(2698))
- Pan, A. D., & Moehle, J. P. (1992). An experimental study of slab-column connections. *Structural Journal*, 89(6), 626–638. <https://doi.org/10.14359/4133>
- Pan, A., & Moehle, J. P. (1989). Lateral displacement ductility of reinforced concrete flat plates. *Structural Journal*, 86(3), 250–258. <https://doi.org/10.14359/2889>
- Park, H. G., & Choi, K.-K. (2007). Strength of exterior slab-column connections subjected to unbalanced moments. *Engineering Structures*, 29(6), 1096–1114. <https://doi.org/10.1016/j.engstruct.2006.08.001>
- Pillai, S. U., Kirk, W., & Scavuzzo, L. (1982). Shear reinforcement at slab-column connections in a reinforced concrete flat plate structure. *Journal Proceedings*, 79(1), 36–42. <https://doi.org/10.14359/10877>
- Regan, P. E. (1981). *Behaviour of reinforced concrete flat slabs*. CIRIA Report No. 89. Construction Industry Research and Information Association.
- Robertson, I., & Johnson, G. (2006). Cyclic lateral loading of nonductile slab-column connections. *ACI Structural Journal*, 103(3), 356. <https://doi.org/10.14359/15313>
- Russell, J. (2015). *Progressive collapse of reinforced concrete flat slab structures* (Doctoral dissertation, University of Nottingham).
- Selby, R. G. (1995). Three-dimensional constitutive relations for reinforced concrete. Doctoral dissertation, University of Toronto (Canada).
- Sherif, A.G. 1996. Behaviour of reinforced concrete flat slabs. Ph.D. thesis, Department of Civil Engineering, The University of Calgary, Calgary, Alta. <https://doi.org/10.11575/PRISM/12049>
- Stamenkovic, A., & Chapman, J. C. (1974). Local strength at column heads in flat slabs subjected to a combined vertical and horizontal loading. *Proceedings of the Institution of Civil Engineers*, 57(2), 205–232. <https://doi.org/10.1680/iicep.1974.4054>
- Tang, M., Yi, W. J., & Liu, L. W. (2019). Investigation on seismic performance of interior slab-column connections subjected to reversed cyclic loading. *Earthquake Engineering and Engineering Vibration*, 39(3), 109–121. (in Chinese).
- Tao, Y., Zhao, W., Shu, J., & Yang, Y. (2021). Nonlinear finite-element analysis of the seismic behavior of RC column-steel beam connections with shear failure mode. *Journal of Structural Engineering*, 147(10), 04021160. [https://doi.org/10.1061/\(ASCE\)ST.1943-541X.0003132](https://doi.org/10.1061/(ASCE)ST.1943-541X.0003132)
- Tian, Y., Jirsa, J. O., Bayrak, O., & Argudo, J. F. (2008). Behavior of slab-column connections of existing flat-plate structures. *ACI Structural Journal*, 105(5), 561. <https://doi.org/10.14359/19939>
- Vecchio, F. J., & Collins, M. P. (1986). The modified compression-field theory for reinforced concrete elements subjected to shear. *ACI Journal*, 83(2), 219–231. <https://doi.org/10.14359/10416>
- Walker, P. R., & Regan, P. E. (1987). Corner column-slab connections in concrete flat plates. *Journal of Structural Engineering*, 113(4), 704–720. [https://doi.org/10.1061/\(ASCE\)0733-9445\(1987\)113:4\(704\)](https://doi.org/10.1061/(ASCE)0733-9445(1987)113:4(704))
- Wood, J. G. (2003). Pipers row car park collapse: Identifying risk. *Concrete*, 37(9), 29–31.
- Zaghlool, E. E. D. R. F. (1971). Strength and behaviour of corner and edge column-slab connections in reinforced concrete flat plates. Doctoral thesis, University of Calgary, Calgary, Canada. <https://doi.org/10.11575/PRISM/13724>
- Zaghlool, E. E. D. R. F., de Paiva, H. R., & Glockner, P. G. (1970). Tests of reinforced concrete flat plate floors. *Journal of the Structural Division*, 96(3), 487–507. <https://doi.org/10.1061/JSDDEAG.0002527>

Publisher's Note

Springer Nature remains neutral with regard to jurisdictional claims in published maps and institutional affiliations.

Ngoc Hieu Dinh is working as a postdoctoral fellow at Soongsil University, Korea. He received his MS and PhD in architectural engineering from Soongsil University. His research interests include seismic design of RC structures and application of fiber reinforced concrete/textile reinforced concrete.

Seung-Hee Kim is a Ph.D. student in the Department of architecture at Soongsil University, Korea. She received BE and MS in the School of Architecture from Soongsil University. Her research interests include design of reinforced concrete structures and vibration analysis in structural members.

Kyung-Kyu Choi is a Professor of Architectural Engineering at Soongsil University, Korea. He received his BE, MS, and PhD in architectural engineering from Seoul National University. He was an associate member of Joint ACI-ASCE Committee 445. He has received the ACI Chester Paul Siess Award for Excellence in Structural Research in 2009 and 2012. His research interests include the shear and seismic design of RC structures and application of fiber reinforced concrete.